available at www.sciencedirect.com

ScienceDirect

journal homepage: www.sciencedirect.com/journal/chinese-journal-of-catalysis

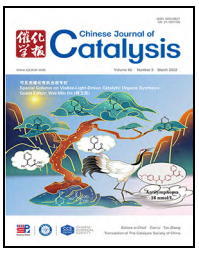

Review

Multifunctional graphene-based composite photocatalysts oriented by multifaced roles of graphene in photocatalysis

Yue-Hua Li, Zi-Rong Tang *, Yi-Jun Xu #

College of Chemistry, State Key Laboratory of Photocatalysis on Energy and Environment, Fuzhou University, Fuzhou 350116, Fujian, China

ARTICLE INFO

Article history:
Received 7 May 2021
Accepted 27 June 2021
Available online 3 February 2022

Keywords:
Graphene
Composite photocatalyst
Optimization strategies
Synthesis method
Multifarious roles of graphene
Photocatalytic applications

ABSTRACT

Graphene (GR), a single-layer carbon sheet with a hexagonal packed lattice structure, has displayed attractive potential and demonstrably become the research focus in artificial photocatalysis due to its enchanting properties in enhancing light absorption, electron transfer dynamics, and surface reactions. Currently, numerous efforts have shown that the properties of GR, which are closely correlated to the photocatalytic performance of GR-based composites are significantly affected by the synthesis methods. Herein, we first introduce the optimization strategies of GR-based hybrids and then elaborate the synthesis of GR-based composite photocatalysts oriented by manifold roles of GR in photoredox catalysis, containing photoelectron mediator and acceptor, improving adsorption capacity, regulating light absorption range and intensity, as well as macromolecular photosensitizer. Beyond that, a brief outlook on the challenges in this burgeoning research field and potential evolution strategies for enhancing the photoactivity of GR-based hybrids is presented and we anticipate that this review could provide some enlightenments for the rational construction and application of multifunctional GR-based composite photocatalysts.

1. Introduction

The discovery made in 2004 triggered tremendous research interest on two-dimensional (2D) honeycomb crystal structure, graphene (GR), in the field of materials science and energy conversion [1]. Especially in photocatalysis, as depicted in Fig. 1, the enhancement in the number of publications on GR and photocatalysis maintains an extraordinary growth rate over the past decade, indicating the extensive attentions focusing on GR-based photocatalysis. Nowadays, multifunctional GR-based photocatalysts, such as GR-semiconductor [2–4], GR-metal [5–8], and GR-organics [9–12] have been widely employed in photocatalytic water splitting [13–17], environmental purification [18–26], carbon dioxide (CO_2) reduction [27–30], and selective organic transformation [31–34] to provide a viable and sustainable strategy to the problems of growing energy requirements and environmental crisis. Owing to the unique and fascinating features of ideal GR [35–38], including 2D flat structure, high theoretical specific surface area, superior optical transmittance, excellent electron conductivity, and good chemical stability, GR has been considered as a promising cocatalyst to enhance the conversion efficiency of solar energy of artificial photosynthesis systems [39,40]. Besides, in some specific photocatalytic systems, GR also is able to act as the macromolecu-

* Corresponding author. E-mail: zrtang@fzu.edu.cn
# Corresponding author. Tel/Fax: +86-591-22865836; E-mail:yjxu@fzu.edu.cn
This work was supported by the National Natural Science Foundation of China (22072023, 21872029, U1463204, 21173045), the Program for National Science and Technology Innovation Leading Talents (00387072), the Award Program for Minjiang Scholar Professorship, the 1st Program of Fujian Province for Top Creative Young Talents and the Natural Science Foundation of Fujian Province (2017J07002, 2019J0106).
DOI: 10.1016/S1872-2067(21)63871-8 | http://www.sciencedirect.com/journal/chinese-journal-of-catalysis | Chin. J. Catal., Vol. 43, No. 3, March 2022

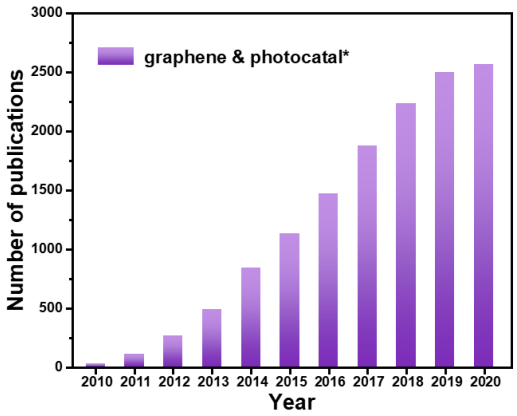

Fig. 1. Number of yearly publications with the subject of "graphene & photocatal*" since 2010. (Using Web of Science, date of search: May 27, 2021.)

lar photosensitizer to generate photoelectrons by itself [41–46].

As is well known, choosing appropriate synthesis method plays a significant role in tailoring the properties of GR-based composites, such as morphology, size, defect structure, and surface/interface properties, which are closely linked to their photocatalytic performance. Hence, enormous efforts have been devoted to exploring proper synthesis methods to construct high-efficiency GR-based composites with desirable architecture [47,48]. Conceptually, these synthesis methods, including hydrothermal/solvothermal method, combustion treatment, low-temperature oil bath method, sol-gel approach, ultrasonication-assisted deposition, microwave-assisted synthesis, photo-assisted reduction, electrochemical deposition, etc., have been divided into ex situ and in situ synthesis methods [49,50].

During the ex situ synthesis process, the precursor of GR, such as graphene oxide (GO), functionalized solvent exfoliated graphene (SEG), commercial Elicarb graphene (EGR) and organic molecules, is mixed with the preformed or commercially available photoactive materials to fabricate GR-based composites. The modification of pre-synthesized individual components and/or post-treatment of as-prepared hybrids are often adopted to reduce the GR precursor and/or optimize the interfacial interaction between GR and photoactive materials. Because desirable morphology and size of pre-selected photoactive ingredient maintain well after ex situ synthesis, the accurate control of microscopic structure of GR-based hybrids, as well as the performance comparison between bare photoactive ingredient and composite photocatalysts, can be implemented [49,50].

As for the in situ synthesis methods, the precursors of GR and photoactive component are preliminarily mixed in a suitable solvent, and then the mixture is treated by thermal, optical, or ultrasonic approaches, during which the photoactive materials with specific structure and morphology, such as nanoparticles (NPs), nanorods (NRs) or nanosheets (NSs) are in situ grown on the surface of GR, thus preparing GR-based composites with intimately contacted interface [51]. In this procedure, 2D GR and its derivatives can not only provide a flexible platform for the well-controlled nucleation and growth of nanocrystals, but also act as the self-assembly template to construct three-dimensional (3D) structured GR gel, which possesses convenient recyclability, multidimensional electron transfer paths, enhanced adsorption capacity and inhibited aggregation of subunits [19,20,52,53]. In addition, GO as the frequently used GR precursor can play a dual role in synthesis template and surfactant to flexibly regulate the morphology, size and defect structure of some specific composites, because –COOH groups on the edge of GO and graphitic domains in the basal plane of GO make it an amphiphile with a hydrophilic periphery and hydrophobic center [5,54].

Thus far, a myriad of reviews related to the GR-based photocatalysis have systematically summarized the classification, synthesis methods, properties, and photocatalytic applications of GR-based composites [39,49–51,55–57]. Given such a situation, in this review, instead of making a typical summary of the fundamental roles, preparation approaches and applications of GR-based composites, we first introduce the optimization strategies of multifunctional GR-based hybrids and then discuss the assembly approaches for synthesizing GR-based composites oriented by the fundamental roles of GR in photocatalysis, containing photoelectron mediator and acceptor, improving adsorption capacity, tailoring light absorption range and intensity and macromolecular photosensitizer (Fig. 2). The key challenges and future perspectives for the further investigations of GR-based photocatalysts are also proposed and we expect that this review can provide reference and new ideas for readers in the rational design and efficient applications of multifunctional GR-based composite photocatalysts.

2. Optimization strategies of GR-based composite photocatalysts

Recently, owing to the numerous advantages of graphene (GR)-based photocatalysis (Fig. 3), GR-based hybrids have been widely applied in photocatalytic hydrogen (H_2) evolution, carbon dioxide (CO_2) reduction, pollutant degradation and nitrogen (N_2) fixation, which have been summarized in Table 1. However, the photocatalytic performance of current GR-based

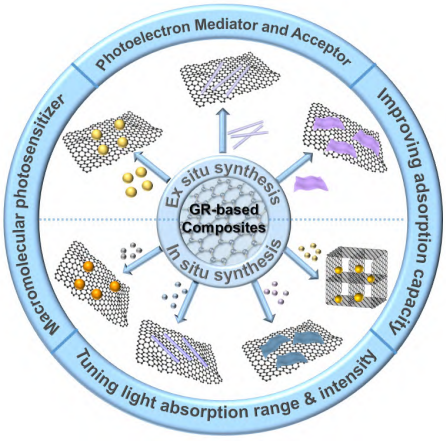

Fig. 2. Illustration of synthesis of GR-based composite photocatalysts oriented by roles of GR in photocatalysis.

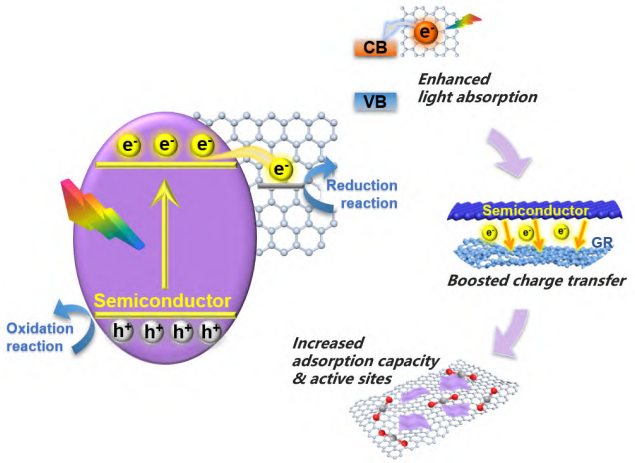

Fig. 3. Numerous advantages of GR-based photocatalysis.

hybrids is still unsatisfactory [40,50]. For the sake of preferable photoconversion efficiency, researchers have developed a variety of optimization strategies, such as decreasing the defect density of GR, chemical doping, optimizing the dimensionality, depositing cocatalysts and optimizing interfacial parameters, which are of great significance to the future design and fabrication of high-performance GR-based hybrids [31,39]. Hence, the optimization strategies of multifunctional GR-based hybrids are briefly introduced before discussing the synthesis of GR-based composites oriented by manifold roles of GR in photocatalysis.

2.1. Decreasing the defect density of GR

Since graphene oxide (GO) with abundant oxygenated functional groups exhibits the attractive properties of low cost, facile preparation and flexible solution processability, it has been extensively used as the precursor of GR in the wet chemical synthesis of GR-based composites [31,40]. However, the numerous oxygen moieties formed in the strong oxidation procedure of GO preparation, such as hydroxyl, epoxy groups and carboxyl unavoidably disrupt the two-dimensional (2D) π-conjugation of electronic structure of GR sheets [39,54]. Although majority of oxygen-containing functional groups can be removed in the subsequent reduction process, the structural defects are unavoidably left on the reduced graphene oxide (rGO), resulting in the decreased the charge carrier mobility and electrical conductivity of rGO as compared to the ideal GR [39,55].

Table 1
Summary of photocatalytic applications of GR-based hybrids in recent years.

Entry	Composite photocatalyst	Light source	Reaction type	Reaction conditions	Ref. Year
1	TNTAs@rGO/MoS_2 [a]	300 W Xe lamp, 320–780 nm	H_2 evolution	vacuum, methanol (10 vol%) or lactic acid (10 vol%)	[58] 2018
2	Ni_2P-FGR [b]	300 W Xe lamp, ≥ 420 nm	H_2 evolution	vacuum, TEOA [c] (10 vol%), Eosin Y	[59] 2018
3	CdS-EGR [d] CdS-rGO	300 W Xe lamp, ≥ 420 nm	H_2 evolution	vacuum, lactic acid (10 vol%)	[60] 2018
4	$CH_3NH_3PbI_3$/rGO	300 W Xe lamp, ≥ 420 nm	H_2 evolution	HI solution	[61] 2018
5	Fe_2O_3/rGO/PCN [e]	300 W Xe lamp, ≥ 420 nm	overall water splitting	H_2O, H_2PtCl_6	[62] 2019
6	graphene/carbon nitride	[1]300 W Xe lamp, ≥ 420 nm [2]LED solar simulator	[1]H_2 evolution [2]photooxidation of 1,4-DHP [f]	[1]N_2, TEOA (10 vol%), H_2PtCl_6 [2]10^{-4} mol/L 1,4-DHP	[63] 2020
7	rGO-CoO_x/$BiVO_4$-Pt-metal sulfides [g]	300 W Xe lamp, ≥ 420 nm	overall water splitting CO_2 reduction to CO	Ar gas flow, H_2O CO_2 gas flow, H_2O	[64] 2016
8	$CsPbBr_3$ QD/GO [h]	100 W Xe lamp, AM 1.5 G	CO_2 reduction to CO	CO_2, ethyl acetate	[65] 2017
9	nanographene-rhenium complex	100 W tungsten lamp, ≥ 490 nm	CO_2 reduction to CO	CO_2, tetrahydrofuran, TEOA	[66] 2017
10	NH_2-rGO/Al-PMOF [i]	125 W medium-pressure mercury lamp	CO_2 reduction to formate	CO_2, TEOA/acetonitrile (*v*:*v* = 1:5)	[9] 2018
11	hypercrosslinked polymer-TiO_2-GR	300 W Xe lamp, ≥ 420 nm	CO_2 reduction to CH_4 and CO	CO_2, H_2O	[30] 2019
12	*N*-doped GR/CdS	350 W Xe lamp, ≥ 420 nm	CO_2 reduction to CO and CH_4	CO_2, H_2O	[28] 2019
13	α-Fe_2O_3/amine-rGO/$CsPbBr_3$	150 W Xe lamp, ≥ 420 nm or AM 1.5 G	CO_2 reduction to CH_4 and CO	CO_2, H_2O	[67] 2020
14	$CsPbBr_3$/USGO/α-Fe_2O_3 [j]	300 W Xe lamp, ≥ 400 nm	CO_2 reduction to CO	CO_2, acetonitrile/H_2O (*v*:*v* = 200:1)	[68] 2020
15	Cs_4PbBr_6/rGO	300 W Xe lamp, ≥ 400 nm	CO_2 reduction to CO	CO_2, ethyl acetate/H_2O (*v*:*v* = 1000:1)	[69] 2020
16	ZnPc/GR/$BiVO_4$ [k]	300 W Xe lamp, ≥ 420 nm	CO_2 reduction to CH_4 and CO	CO_2, H_2O	
17	TaON@GR	300 W Xe lamp, ≥ 420 nm	CO_2 reduction to CH_4	CO_2, H_2O	[27] 2020
18	transition metal hydroxide-GR [l]	300 W Xe lamp, ≥ 420 nm	CO_2 reduction to CO	CO_2, TEOA, acetonitrile/H_2O (*v*:*v* = 3:2), $[Ru(bpy)_3]Cl_2·6H_2O$	[48] 2020
19	Co-metal-organic layers@GR	Blue LED, λ = 450 nm	CO_2 reduction to CO	CO_2, TEOA, acetonitrile/H_2O (*v*:*v* = 4:1), $[Ru(phen)_3]$ $(PF_6)_2$	[70] 2021
20	single Co atoms/GR	300 W Xe lamp, ≥ 420 nm	CO_2 reduction to CO	CO_2, acetonitrile/TEOA/H_2O (*v*:*v*:*v* = 3:1:1), $[Ru(bpy)_3]Cl_2·6H_2O$	[71] 2018

(To be continued)

Table 1 (continued)

Entry	Composite photocatalyst	Light source	Reaction type	Reaction conditions	Ref. Year
21	MIL-53(Fe)-GR	500 W Xe lamp, ≥ 400 nm	photooxidation of benzyl alcohols	CCl_4, benzyl alcohols	[72] 2016
22	Eu-based MOF/GO	5 W LED	photooxidation of benzyl alcohol	N_2, benzyl alcohol, acetonitrile/H_2O (v:v = 2:1)	[12] 2017
23	Cu_2O-MoS_2/GR	24 W compact fluorescent bulb	oxidative C–C bond formation	*N*-aryl-tetrahydroisoquinoline and nitromethane	[73] 2017
24	GR/Ag/α-Al_2O_3	0.5 W laser, 514.5 nm	photo-epoxidation of ethylene	C_2H_4 and air	[74] 2018
25	Ni_2P-graphene-TiO_2	300 W Xe lamp, ≥ 420 nm	photooxidation of benzyl alcohol coupled with H_2 evolution	N_2, benzyl alcohol solution	[75] 2019
26	Cu_2S:NiS_2@C/rGO	300 W Xe lamp, 400–800 nm	[1]chan-Lam coupling reaction [2]cyclization reaction [3]oxidative homocoupling reaction	[1]phenylboronic acid and imidazole, methanol/H_2O (v:v = 3:1) [2]1,2-phenylenediamine, aromatic aldehyde, ethanol [3]benzylamine, acetonitrile	[76] 2021
27	CdS/GR	500 W tungsten-halogen lamp	photodegradation of Rhodamine B	rhodamine B solution	[77] 2017
28	BiOI/GO	5 W LED, ≥ 400 nm	photodegradation of phenol	phenol solution	[78] 2020
29	GR/ZnO	125 W, λ = 365 nm	photodegradation of Rhodamine B, methyl orange, and Methylene blue	rhodamine B solution, methyl orange solution, and Methylene blue solution	[79] 2021
30	Fe_3O_4/polypyrrole/rGO	250 W tungsten-halogen lamp (two)	degradation of acetaminophen	acetaminophen solution, pH = 6.7 ± 0.2	[80] 2021
31	TiO_2/g-C_3N_4/GR	300 W Xe lamp	reduction of nitrobenzene	N_2, nitrobenzene, methanol solution	[81] 2017
32	g-C_3N_4/aromatic diimide/GR	2 kW Xe lamp, ≥ 420 nm	H_2O_2 production	O_2, H_2O	[82] 2016
33	Bismuth-graphene	direct sunshine (0.039–0.048 W cm^{-2})	[1]degradation of Methyl orange [2]reduction of Cr (VI)	methyl orange solution (pH = 2)	[83] 2017
34	3DG-organic hybrid [m]	300 W Xe lamp, ≥ 420 nm	reduction of 4-nitroaniline reduction of Cr (VI)	N_2, 4-nitroaniline solution, TEOA N_2, Cr (VI) solution, TEOA	[19] 2018
35	$Ti_3C_2T_x$/GO-Eosin Y	300 W Xe lamp, ≥ 420 nm	reduction of Cr (VI)	N_2, Cr (VI) solution (pH = 7), TEOA	[84] 2019
36	Carbon QDs/GR aerogel [n]	300 W Xe lamp, 200–780 nm	reduction of Cr (VI)	N_2, Cr (VI) solution, TEOA	[20] 2019
37	NCQDs/GA [o]	300 W Xe lamp, ≥ 420 nm	reduction of Cr (VI)	N_2, Cr (VI) solution, TEOA	[18] 2019
38	CdSe QDs/graphene/TiO_2	350 W Xe lamp, ≥ 420 nm	E. coli disinfection	e. coli, 0.9% NaCl solution, 37 °C	[85] 2018
39	GR/AgBr/Ag aerogel	300 W Xe lamp, ≥ 400 nm	E. coli disinfection	e. coli, phosphate-buffered saline buffer (pH = 7.4), 25 °C	[52] 2019
40	GO@polyoxometalate	300 W Xe lamp	N_2 fixation	N_2, H_2O, Nessler's reagent	[86] 2019
41	rGO/red phosphorus	300 W Xe lamp, ≥ 400 nm	N_2 fixation	N_2, H_2O, Nessler's reagent	[87] 2021

Note: [a] TNTAs@rGO/MoS_2 refers to TiO_2 nanotube Arrays@rGO/MoS_2. [b] Ni_2P-FGR refers to Ni_2P-functionalized single-layer GR. [c] TEOA refers to triethanolamine. [d] CdS-EGR refers to CdS-Elicarb GR. [e] Fe_2O_3/rGO/PCN refers to Fe_2O_3/rGO/polymeric carbon nitride. [f] 1,4-DHP refers to 1,4-dihydro-2,6-dimethylpyridine-3,5-dicarboxylate. [g] metal sulfides refers to $CuGaS_2$, $CuInS_2$, Cu_2ZnGeS_4, and Cu_2ZnSnS_4. [h] $CsPbBr_3$ QD/GO refers to $CsPbBr_3$ quantum dots/GO. [i] NH_2-rGO/Al-PMOF refers to amine-functionalized graphene/porphyrin-based metal-organic framework. [j] $CsPbBr_3$/USGO/α-Fe_2O_3 refers to $CsPbBr_3$/ultrathin and small-size GO/α-Fe_2O_3. [k] ZnPc/GR/$BiVO_4$ refers to zinc phthalocyanine/GR/$BiVO_4$. [l] Transition metal hydroxide-GR refers to $Ni(OH)_2$-GR, $Fe(OH)_3$-GR, $Cu(OH)_2$-GR and $Co(OH)_2$-GR. [m] 3DG-organic hybrid refers to three-dimensional graphene-Eosin Y(or Rose Bengal). [n] carbon QDs/GR aerogel refers to carbon quantum dots/GR aerogel. [o] NCQDs/GA refers to nitrogen-doped carbon quantum dots/GR aerogel.

In this context, it is necessary to decrease the defect density of GR by exploring efficient synthesis methods of defect-free or defect-few GR, such as solvent exfoliation, electrochemical exfoliation and thermal exfoliation method, etc [49,57]. Recently, solvent-exfoliated graphene (SEG) synthesized by the exfoliation of graphite in organic solvents with the aid of sonication and commercial GR (e.g., Elicarb GR obtained from Thomas Swan Co. Ltd. of UK, GO dispersion obtained from XFNANO of China) with decreased defect density have been employed to replace rGO for the construction of GR-based hybrids, which exhibit enhanced charge separation and transport efficiency, as well as superior photoactivity as compared to rGO-based hybrids [54,60,88,89]. Notably, due to the scantiness of oxygenated functional groups on their surface, above-mentioned defect-free or defect-few GR sheets possess hydrophobic nature and poor dispersion in aqueous solution, which reduce the processability of them and thus restrain their utilization in wet chemistry synthesis of GR-based hybrids. For the purpose of processing defect-free or defect-few GR in benign solvents, it is necessary to modify their surface with surfactants or solvent-liking polymers, by which the surface properties of them, such as hydrophilicity and surface charge can be effectively regulated [54,60]. In addition, considering the fact that residual insulating surfactants or polymers may disrupt the π-conjugation of GR sheets and thus influence the electronic properties of GR sheets, the balance between electrical conductivity and surface properties of GR needs to be struck by further optimizing the synthetic procedure of GR [54,60].

2.2. Chemical doping

Chemical doping as a feasible means can not only modulate the local charge distribution and state density of GR, but also introduce additional catalytic sites to facilitate the adsorption and activation of reactant molecules, thus enhancing the photoactivity of GR-based hybrids [28,90,91]. Conceptually, chemical doping is divided into surface transfer doping and substitutional doping. Surface transfer doping occurs through the electron exchange between GR and chemical species, such as atomic hydrogen, potassium, bromine, iodine and nitrogen dioxide adsorbed on the surface of GR, which cannot change the intrinsic structure of GR [92,93]. Since the dopants may desorb from the surface of GR and react with H_2O or oxygen (O_2), GR doped by this way is unstable. In contrast, substitutional doping can realize the incorporation of heteroatoms (*e.g.,* N atoms, S atoms, P atoms and B atoms) in carbon network of GR, resulting in the enhanced stability of doped GR [91,94–97].

However, there are still some open questions in the controllable synthesis and photocatalytic applications of doped GR. Firstly, it is difficult to precisely control the surface adsorption of dopants and the number of doped heteroatoms in GR. Secondly, the synthesis process of doped-GR (e.g., ion implantation and nitrogen plasma treatment) may produce defects, which serve as the recombination centers of photoinduced charge carriers and affect the photocatalytic activity. Hence, it is necessary to control the number and distribution of these defects in doped-GR. Thirdly, the doping mechanism, as well as the relationship between doping and band gap opening of GR are not thoroughly understood [90,91]. The methodical investigation on aforementioned issues is conducive to understanding the contribution of chemical doping to photocatalytic performance improvement and achieving the accurate control of chemical doping of GR.

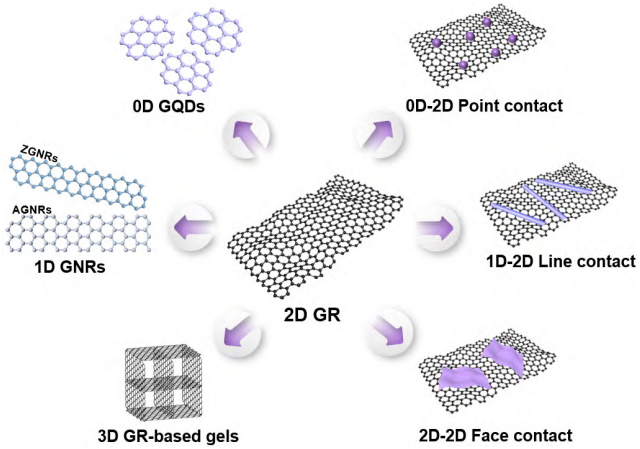

Fig. 4. Diagram of the optimization of dimensionality of GR (left) and GR-based hybrids with different structure (right).

2.3. *Optimizing the dimensionality*

For GR-based photocatalysis, it has been demonstrated that optimizing the dimensionalities of GR and photoactive components makes a positive impact on enhancing the performance of photocatalytic system [31]. As depicted in Fig. 4, the zero-dimensional graphene quantum dots (0D GQDs), one-dimensional graphene nanoribbons (1D GNRs) and three-dimensional (3D) GR-based gels as the derivates of 2D GR species have elicited incessant attentions for constructing high quality GR-based hybrids [98].

Among them, 0D GQDs, which are constitutive of one- or few-layer GR sheets with small lateral dimensions less than 10 nm (Fig. 5(a)) exhibit great potential in the field of photocatalysis, cell imaging and biomedicine due to their advantages of high electron reservation capability, unique optical properties,

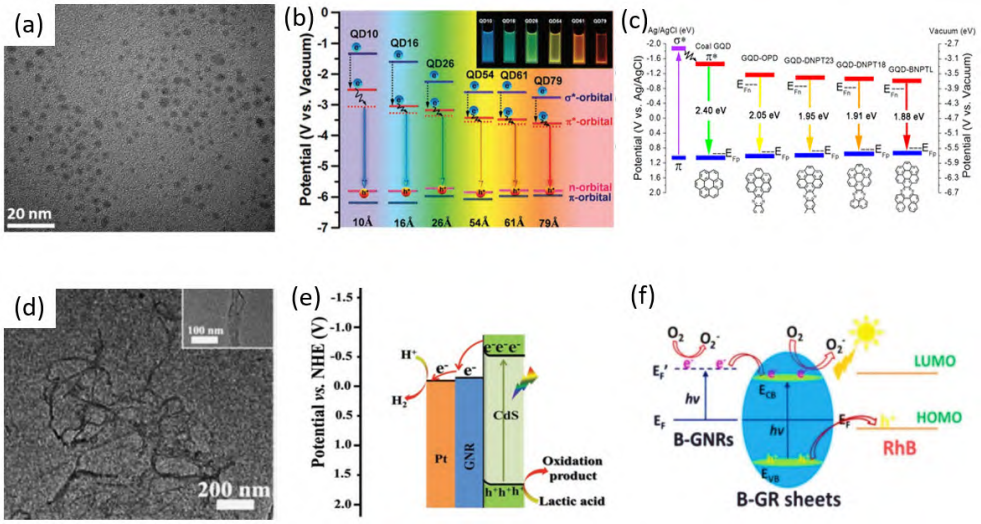

Fig. 5. (a) TEM image of GQDs. Reprinted with permission from Ref. [104], Copyright 2017, Elsevier. (b) Diagram of bandgap structures of GQDs with different pore sizes. Reprinted with permission from Ref. [105], Copyright 2016, American Chemical Society. (c) Diagram of bandgap structures of GQDs with different chemical groups. Reprinted with permission from Ref. [106], Copyright 2018, American Chemical Society. (d) TEM image of GNRs (e) Photoinduced charge carrier transport process of CdS/GNR/Pt. (d,e) Reprinted with permission from Ref. [107], Copyright 2019, Wiley-VCH. (f) Diagram of photocatalytic mechanism of RhB degradation over N-GNRs/B-GR sheets. Reprinted with permission from Ref. [108], Copyright 2014, Royal Society of Chemistry.

chemical inertness and low cytotoxicity [55,98,99]. The abundant oxygen-containing functional groups, such as hydroxyl, carboxyl, and epoxy groups on the edges of GQDs impart them with good water solubility and functionalization possibilities, which facilitate the synthesis of multifunctional GQDs-based photocatalysts through wet chemical process [100,101]. Unlike GR with zero bandgap, the bandgap of 0D GQDs can be opened and regulated by tuning their size and surface chemistry because of the quantum confinement effect, which have been revealed in Figs. 5(b) and (c). In addition, considering that GQDs exhibit the size-dependent light absorption properties in ultraviolet (UV) light region and the tail of light absorption can be extended to visible light range, GQDs could act as photosensitizer or photoactive materials in various photoredox systems. Another engaging feature of GQDs is their photoluminescence (PL) properties, which depend on the size of GQDs, the type and pH of solvent, along with the excitation wavelength. Owing to the up-conversion luminescence (UCPL) properties of a part of luminescence GQDs, they could act as the photon mediator to realize the conversion of lower-energy photons to higher-energy photons, thus facilitating the utilization of visible light and even infrared light [102,103].

1D GNRs obtained by cutting GR sheets into strips with a narrow width less than dozens of nanometers (Fig. 5(d)) exhibit inherent merits of high specific surface area, good light absorption capability, decreased defect density and abundant active edges [107,109]. As exhibited in Fig. 4, according to the termination type of GNRs, they can be categorized into zigzag GNRs (ZGNRs) and armchair GNRs (AGNRs). Theoretical calculations demonstrated that the different boundary conditions of ZGNRs and AGNRs endow them with diverse electronic properties, which can be optimized by heteroatom doping and molecular functionalization [55,110,111]. Specifically, ZGNRs possess metallic characteristics while AGNRs possess metallic or semiconducting characteristics, which make GNRs possess tunable band gap and good electrical conductibility, thus acting as the photosensitizer or photoelectron mediator in specific composite photocatalysts, which has been depicted in Figs. 5(e) and (f) [107,108,112–114].

Besides, because of the strong van der Waals force between GR layers, 2D GR sheets incline to stack during the synthesis process, which could affect the specific surface area and electronic properties of GR, thereby restraining the function of GR in enhancing the photoactivity of other components [20,52]. Given this situation, 3D GR-based gels, which possess interconnected porous structure and macroscopic block appearance, have been constructed to alleviate the aggregation of GR sheets [18,19,115]. The porous structure of 3D GR-based gels not only provides multidimensional channels to boost the mass and electron migration, but also inhibits the aggregation of other ingredients to expose more catalytic sites for efficient adsorption and activation of reactant molecules. In terms of the practical applications, the macroscopic block appearance endows the convenient separation and recycling of 3D GR-based gels [20,52,84].

In addition to tuning the dimensionality of GR derivates, the regulation of dimensionality of other ingredients, such as semiconductor and metal-organic-frameworks (MOFs) has also been probed [4,116]. As depicted in Fig. 4, compared with the point contact and line contact in GR-based hybrids with 0D-2D and 1D-2D structure, the face contact in 2D-2D GR-based hybrids is beneficial to improve the interfacial area and shorten the charge transport paths, thereby improving the photocatalytic performance [117,118]. Hence, GO sheets with oxygen-containing functional groups have been simultaneously used as the 2D platform and surfactant to assemble other ingredients with flexibly controllable morphology. Besides, the pre-modification of GR sheets with rich functional groups (*i.e.,* amide groups) makes GR sheets play a similar role in regulating and stabilizing the morphology of other components as GO, thus fostering the photoactivity enhancement of GR-based hybrids [119,120].

2.4. Depositing cocatalysts

Owing to the inherent and unique properties of ideal GR, GR has been considered as the highly-efficient cocatalyst to boost the lifetime and migration rate of photoexcited charge carriers, improve the adsorption of reactant molecules, as well as regulate the light absorption range and intensity of GR-based composites [40,50]. However, the unavoidable recombination of electron-hole pairs and shortage of catalytic sites still severely restrict the further improvement of photoactivity and regulation of selectivity of GR-based hybrids [31,39]. In order to alleviate above problems, other cocatalysts, such as single-atomic cocatalyst, bimetallic cocatalyst, layered transition metal disulfide and transition metal oxide/phosphate/sulfide have been deposited with GR on semiconductors to construct dual- or multi- cocatalysts systems, which have been summarized in Fig. 6 [64,121]. As shown in Path I and III in Fig. 6, coupling another reduction cocatalyst (e.g., MoS_2, NiS_2, Ag_2O, CuS) or oxidation cocatalyst (e.g., RuO_2, CoO_x, MnO_2) with GR could construct multi-level charge transport pathways to facilitate the charge separation dynamics and thereby improve the photoactivity of GR-based hybrids [121–127]. When the plasmonic metal (e.g., Au, Ag, Bi) is selected as another cocatalyst, the multi-channel charge transfer paths (Path II in Fig. 6) formed by plasmonic electrons migration in GR-based hybrids are also beneficial to the charge transfer and photoactivity enhancement [128–130]. In another aspect, the decoration of metal-based cocatalysts can provide abundant surface active sites for some specific photoredox reactions, which could play a dual role in regulating

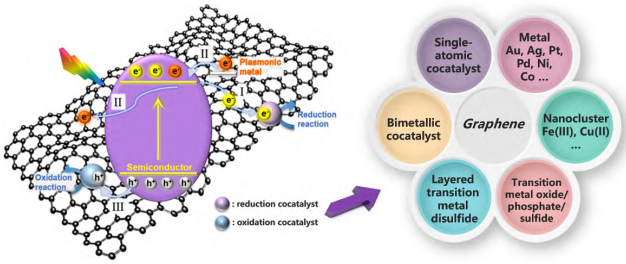

Fig. 6. Diagram of charge transfer pathways of GR-based dual-cocatalysts system and different types of cocatalysts that coupled with GR.

the activity and selectivity of GR-based hybrids [13,51,131].

Additionally, it is worth noting that the parameters of cocatalysts (e.g., morphology, size and exposed crystal face) significantly influence their efficacy and the random distribution of dual- or multi- cocatalysts on semiconductors ineluctably enhances the recombination possibility of charge carriers and results in undesirable side or back photoreactions [132]. Hence, rational regulation of cocatalysts parameters and the controllable deposition of spatially separated dual- or multi-cocatalysts have been taken into consideration, thus optimizing the architecture and photocatalytic performance of GR-based hybrids [124,131,133].

2.5. Optimizing interfacial parameters

Since the charge transfer between GR and other components in hybrids mainly occurs in the interfacial region, optimizing interfacial parameters of GR-based hybrids, such as increasing the interfacial contact, tuning the interfacial composition and band bending alignment is of great significance to

Table 2
Summary of synthesis methods of GR-based hybrids.

Entry	Composite photocatalyst	Precursor of GR	Precursor of other component	Preparation method	Ref. Year
1	GR@TiO_2	GO prepared by modified Hummers' method	tetrabutyl orthotitanate	GR@TiO_2 prepared by sol-gel process (in the mixture of ethanol, benzyl alcohol and H_2O), calcination (N_2, 450 °C, 2 h)	[117] 2014
2	TiO_2/GR	GO prepared by modified Hummers' method	commercial TiO_2	TiO_2/GR prepared by mechanical mixing of GO and TiO_2 in 1-butyl alcohol (ultrasonication 0.5 h), catalysts dried at 100 °C	[139] 2017
3	TiO_2/GR	GO prepared by conventional Hummers' method	P25	GO and P25 mixed in NH_3 solution (60 °C, 2 h), GO reduced by N_2H_4, catalysts dried at 200 °C	[140] 2017
4	TiO_2@rGO	GO prepared by modified Hummers' method	P25	GO and P25 mixed in ethanol, GO reduced under ultraviolet light (N_2)	[141] 2017
5	TNTAs@rGO/MoS_2	GO prepared by modified Hummers' method	Ti foil	TNTAs prepared by anodic oxidization of Ti foil, rGO electrodeposited on TNTAs, MoS_2 photodeposited on TNTAs@rGO	[58] 2018
6	TiO_2/graphene	graphite powder	titanium tetra-*n*-butoxide	graphene obtained by chemical exfoliation of graphite in titanium tetra-n-butoxide (60 °C, 4 h, N_2), TiO_2 prepared by sol-gel method	[142] 2018
7	hypercross-linked polymer-TiO_2-GR	GO prepared by modified Hummers' method	lamellar protonated titanate	solvothermal method (lamellar protonated titanate, GO, isopropyl alcohol, fluoric acid, glucose, 180 °C, 12 h)	[30] 2020
8	ZnO/rGO	GO prepared by modified Hummers' method	$Zn(CH_3COO)_2{\cdot}2H_2O$	ZnO/rGO prepared by solvothermal method (ethanol, NaOH, 160 °C, 24 h)	[143] 2016
9	ZnO nanoring/rGO	GO prepared by modified Hummers' method	$Zn(CH_3COO)_2{\cdot}2H_2O$	ZnO nanoring/rGO prepared by hydrolysis and chemical etching approach (cetyltrimethylammonium bromide, dimethyl sulfoxide, heat in an oven, 70 °C, 1.5 h)	[144] 2017
10	ZnO/Thermally reduced graphene	GO prepared by modified Hummers' method	$Zn(CO_3)_2(OH)_6$	ZnO/thermally reduced graphene synthesized by ball milling of GO and $Zn(CO_3)_2(OH)_6$, calcination (inert gas, 400 °C, 2 h)	[145] 2019
11	GR/ZnO	GO prepared by modified Hummers' method	$Zn(CH_3COO)_2{\cdot}2H_2O$	GR/ZnO prepared by dissolving $Zn(CH_3COO)_2{\cdot}2H_2O$ in GO suspension and stirring for 3 h, GO reduced by adding N_2H_4 and stirring for 3 h	[146] 2020
12	ZnO-GO	GO prepared by modified Hummers' method	$Zn(CH_3COO)_2{\cdot}2H_2O$	ZnO-GO prepared by ultrasonic mixing and freeze-drying	[147] 2020
13	WO_3/rGO	GO prepared by modified Hummers' method	$Na_2WO_4{\cdot}2H_2O$, NaCl	WO_3/rGO prepared by hydrothermal method (180 °C, 15 h)	[148] 2018
14	SnO_2 microspheres-GOs	GO prepared by modified Hummers' method	$Na_2SnO_3{\cdot}4H_2O$	SnO_2 microspheres-GOs prepared by hydrothermal method (180 °C, 15 h)	[149] 2016
15	SnO_2-rGO	GO prepared by modified Hummers' method	$SnSO_4$	$SnSO_4$ first dissolved in H_2SO_4 and GO solution, then reduced by ultraviolet light	[150] 2017
16	Cu_2O-dG [a]	Alginic acid sodium salt	$Cu(NO_3)_2{\cdot}H_2O$	dG prepared by alginate pyrolysis (inert gas, 200 °C, 2 h; 900 °C, 2 h), Cu_2O-dG prepared by heating the mixture of $Cu(NO_3)_2{\cdot}H_2O$, dG and ethylene glycol at 900 °C for 2 h	[151] 2018
17	GO/TiO_2/Bi_2WO_6	GO manufactured by the XFNANO of China	$Bi(NO_3)_3{\cdot}5H_2O$, $Na_2WO_6{\cdot}2H_2O$	GO/TiO_2/Bi_2WO_6 prepared by hydrothermal process (160 °C, 15 h)	[89] 2019
18	rGO/BiOBr	GO prepared by modified Hummers' method	$Bi(NO_3)_3{\cdot}5H_2O$, KBr	GO reduced to rGO by l-ascorbic acid, rGO/BiOBr obtained by hydrothermal process (160 °C, 12 h)	[152] 2019
19	ZnPc/GR/$BiVO_4$	Polyacrylic weak-acid cation-exchanged resin	$BiCl_3$, $NaVO_3$	GR prepared by in situ self-generating template route, $BiVO_4$ prepared by hydrothermal process (120 °C, 12 h), GR/$BiVO_4$ obtained by hydroxyl-induced assembly method (150 °C, 4 h), ZnPc/GR/$BiVO_4$ obtained by assembly process in absolute ethyl alcohol	[153] 2020

(To be continued)

Table 2 (continued)

Entry	Composite photocatalyst	Precursor of GR	Precursor of other component	Preparation method	Ref. Year
20	GNs-CdS QDs [b]	GO prepared by modified Hummers' method	Na_2S, $CdCl_2$	CdS QDs prepared by heat injection method, GNs-CdS QDs prepared by layer-by-layer self-assembly method	[154] 2014
21	CdS-rGO	GO prepared by modified Hummers' method	$Cd(CH_3CO_2)_2{\cdot}2H_2O$, thiourea	CdS-rGO prepared by hydrothermal method (180 °C, 12 h)	[155] 2017
22	CdS/*m*-TiO_2/G [c]	GO prepared by modified Hummers' method	$Cd(CH_3COO)_2{\cdot}2H_2O$, dimethyl sulfoxide	*m*-TiO_2 prepared by sol-gel and hydrothermal process, CdS/*m*-TiO_2/G prepared by solvothermal method (180 °C, 12 h)	[156] 2018
23	Ni-NG/CdS [d]	GO prepared by modified Hummers' method	commercial CdS	Ni-NG prepared by impregnation and calcination process (NH_3, 750 °C, 1 h), Ni-NG/CdS prepared by self-assembly route	[157] 2018
24	N-doped GR/CdS	GO prepared by modified Hummers' method	$CdCl_2$, sodium citrate, ammonia, thiourea	CdS/SiO_2 prepared by using SiO_2 as sacrificial template, *N*-doped GR deposited on CdS/SiO_2 by a chemical vapor deposition at 700 °C	[28] 2019
25	$NiS_x/Cd_{0.8}Zn_{0.2}S$/rGO	GO prepared by modified Hummers' method	$Zn(NO_3)_2{\cdot}6H_2O$, $CdCl_2{\cdot}2.5H_2O$, $Ni(NO_3)_2{\cdot}6H_2O$, glucose, L-cysteine	$NiS_x/Cd_{0.8}Zn_{0.2}S$/rGO prepared by hydrothermal method (160 °C, 2 h)	[158] 2018
26	$ZnIn_2S_4$-GR	GO prepared by modified Hummers' method	$ZnCl_2$, $InCl_3{\cdot}4H_2O$, thioacetamide	$ZnIn_2S_4$-GR prepared by refluxing wet chemistry method (95 °C, 5 h)	[116] 2014
27	CdS/$ZnIn_2S_4$/rGO	GO prepared by modified Hummers' method	$Cd(NO_3)_2$, sulfur powder, ethanediamine, thioacetamide, In $(NO_3)_3$, $Zn(CH_3COO)_2$	CdS/$ZnIn_2S_4$ prepared by solvothermal method, GO reduced by N_2H_4 and NH_3 solution (95 °C, 1 h), CdS/$ZnIn_2S_4$/rGO prepared by electrostatic self-assembly process	[159] 2017
28	rGO/$ZnIn_2S_4$	GO prepared by modified Hummers' method	$ZnSO_4{\cdot}7H_2O$, $In(NO_3)_3{\cdot}4H_2O$, thioacetamide	rGO/$ZnIn_2S_4$ prepared by alcohothermal method (ethanol, glycerol, 180 °C, 12 h)	[160] 2019
29	Ag:$ZnIn_2S_4$/rGO	GO prepared by modified Hummers' method	$In(OOCCH_3)_3$, $Zn(CH_3COO)_2{\cdot}2H_2O$	Ag:$ZnIn_2S_4$/rGO prepared by hydrothermal method (180 °C, 12 h)	[161] 2020
30	$CsPbBr_3$ QDs/GO	GO prepared by modified Hummers' method	Cs-oleate, $PbBr_2$	$CsPbBr_3$ QDs and $CsPbBr_3$ QDs/GO prepared by anti-solvent precipitation method	[65] 2017
31	$LaCoO_3$/attapulgite/rGO	GO prepared by modified Hummers' method	$La(NO_3)_3{\cdot}6H_2O$ $Co(NO_3)_2{\cdot}6H_2O$	$LaCoO_3$/attapulgite prepared by sol-gel method and calcination (600 °C, 2 h), $LaCoO_3$/attapulgite/rGO prepared by self-assembly process	[162] 2018
32	$CsPbBr_3$/USGO/α-Fe_2O_3	GO prepared by modified Hummers' method	Cs_2CO_3, $PbBr_2$	$CsPbBr_3$ prepared by heat injection method, USGO/α-Fe_2O_3 prepared by hydrothermal process (180 °C, 12 h), $CsPbBr_3$/USGO/α-Fe_2O_3 prepared by electrostatic self-assembly process	[68] 2020
33	α-Fe_2O_3/Amine-rGO/$CsPbBr_3$	GO prepared by modified Hummers' method	Cs-oleate, $PbBr_2$	α-Fe_2O_3 nanorod array film prepared by hydrothermal process, α-Fe_2O_3/Amine-rGO prepared by electrostatic self-assembly process, α-Fe_2O_3/Amine-rGO/$CsPbBr_3$ prepared by solvent evaporation deposition approach	[67] 2020
34	$Cs_2AgBiBr_6$/rGO	GO prepared by modified Hummers' method	$BiBr_3$, AgBr, HBr acid, CsBr	$Cs_2AgBiBr_6$ prepared by oil bath method, $Cs_2AgBiBr_6$/rGO prepared by photoreduction process	[163] 2020
35	MIL-LIC-1(Eu)@GO	GO prepared by modified Hummers' method	$EuCl_3{\cdot}6H_2O$, 2-aminotere-phthalic acid	MIL-LIC-1(Eu) prepared by solvothermal method (*N*,*N*′-dimethylformamide, 120 °C, 20 h), MIL-LIC-1(Eu)@GO prepared by heating the mixture of GO/H_2O and MIL-LIC-1(Eu)/H_2O at 120 °C for 12 h	[12] 2017
36	NH_2-rGO/Al-PMOF	Graphenea	$AlCl_3$, 4-carboxyphenyl porphyrin	NH_2-rGO obtained by solvothermal method (ammonia water, 180 °C, 10 h), NH_2-rGO/Al-PMOF obtained by hydrothermal method (180 °C, 24 h),	[9] 2018
37	Co-MOL@GO [e]	GO prepared by modified Hummers' method	$CoCl_2{\cdot}6H_2O$, 5-(1H-1,2,4-triazol-1-yl) isophthalic acid	Co@GO obtained by oil bath (80 °C , 24 h), Co-MOL@GO obtained by solvothermal method (*N*,*N*′-dimethylformamide, H_2O, acetic acid, 130 °C, 4 h)	[70] 2021
38	rGO-TpPa-1-COF [f]	GO prepared by modified Hummers' method	1,3,5-Triformylphloroglucinol, *p*-Phenylenediamine	rGO-TpPa-1-COF obtained by heating the mixture of precursors, *N*,*N*′-dimethylformamide and acetic acid at 120 °C for 72 h	[164] 2020

Note: [a] Cu_2O-dG refers to Cu_2O-defective GR. [b] GNs-CdS QDs refers to GR nanosheets-CdS QDs. [c] CdS/m-TiO_2/G refers to CdS/mesoporous TiO_2/GR. [d] Ni-NG/CdS refers to Ni-N-doped graphene/CdS. [e] Co-MOL@GO refers to Co-metal-organic layers@GO. [f] rGO-TpPa-1-COF refers to rGO-TpPa-1-covalent organic frameworks.

foster the charge transfer and thus improve the photoactivity of GR-based hybrids [134,135].

For *in situ* synthesis methods, as the most commonly used precursor of GR, GO with plentiful oxygen-containing functional groups possesses good solution processability and unique structure-directing role, which endow the *in situ* nucleation and growth of other components with controllable morphology on its surface, thus realizing the intimate interfacial contact be-

tween GR and other components [39,56,136]. In addition to enhancing the interfacial contact of GR-based hybrids, optimizing the interfacial composition also plays an important role in promoting the photoexcited electrons transport. For example, a simple and general strategy of introducing a series of metal ions or metal nanoparticles as generic interfacial mediator into the interfacial layer between GR and semiconductor has been explored to optimize the charge transport paths from semiconductor to GR and thus boost the interfacial charge separation and migration in GR-based hybrids. Moreover, the addition of generic interfacial mediator can partly counterbalance the light shielding effect of GR, thus synergistically improving the photocatalytic performance of semiconductor-metal-GR hybrids [137,138].

For ex situ synthesis methods, the surface modification of GR and pre-synthesized components can not only make them exhibit opposite surface charge to strengthen electrostatic interaction, but also harness the reactions of different functional groups to realize the covalent link between them and thus boosting the interfacial interactions of GR-based hybrids [119,120]. Except for the premodification of GR and other components, the post-treatments of GR-based hybrids by thermal, chemical or optical approach have also been utilized to reduce the precursor of GR and/or further optimize the interfacial interaction between GR and other components [39,40,49].

3. Synthesis of GR-based composite photocatalysts oriented by roles of GR in photocatalysis

On account of the unique and engaging properties of ideal GR, GR plays vital roles in three key steps in photocatalysis, namely light absorption, charge separation and surface reaction to improve the solar-to chemical conversion efficiency of photocatalytic systems [39]. In regard to light absorption, GR can not only enhance the light adsorption intensity and broaden the light adsorption range of photoactive component, but also act as the photosensitizer to generate electrons by itself [44–46]. Owing to its electron conductivity, GR is considered as an efficient cocatalyst to boost the capture and shuttle of charge carries [50,116]. Furthermore, the high specific surface area and unique surface properties of GR endow it strong adsorption capability of specific reactant molecules, thus facilitating the surface reactions [27,84]. For the purpose of taking full use of diversiform roles of GR in photocatalysis, various synthesis methods of GR-based hybrids have been developed and optimized (Table 2). Considering that many reviews have summarized the synthesis methods of GR-based hybrids, we will introduce the synthesis of GR-based hybrids from a new perspective, which is oriented by the role of GR in photocatalysis, thereby providing reference and inspiration for future works.

3.1. Photoelectron mediator and acceptor

As the most frequently used cocatalyst for photocatalysis, GR has been widely proved as the photoelectron mediator and acceptor in a variety of photocatalytic systems due to its inherent electronic conductivity. In this section, we will discuss how to give full play to the role of GR as the photoelectron mediator and acceptor in photocatalytic systems through decreasing the defect density of GR, adjusting the dimensionality of GR and other components, along with optimizing the structure of GR-based composites.

For example, Xu *et al.* [116] have used a low-temperature refluxing wet chemistry method to prepare $ZnIn_2S_4$/GR composites with close interfacial contact caused by the *in situ* synthesis process. As shown in Figs. 7(a) and (b), due to the "structure-directing" function of GO, the morphology of $ZnIn_2S_4$ changed from irregular microparticles to 2D nanosheets (NSs) after introducing GO as the precursor of GR during the synthesis process. $ZnIn_2S_4$/GR composites exhibit higher photoactivity for selective reduction of a series of nitroaromatics with dif-

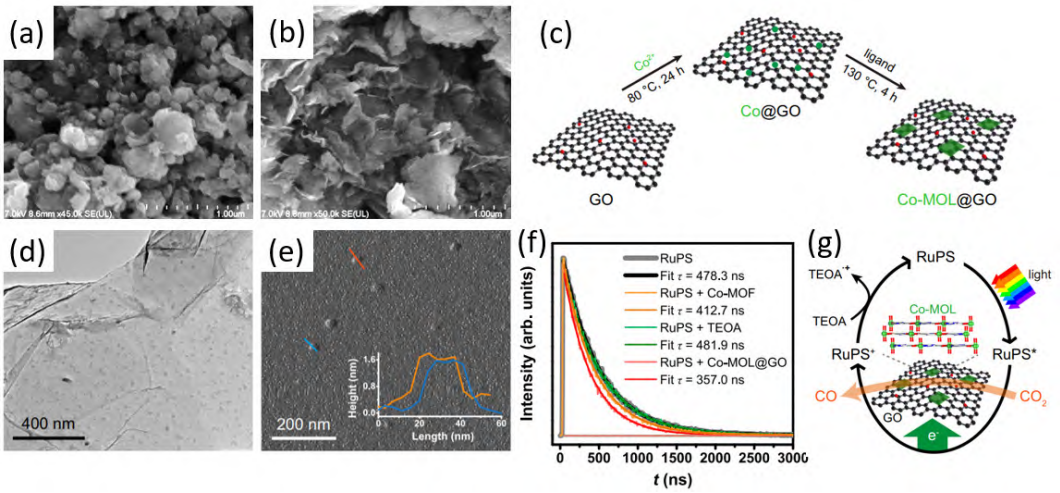

Fig. 7. SEM images of blank $ZnIn_2S_4$ (a) and $ZnIn_2S_4$-GR composite (b). (a,b) Reprinted with permission from Ref. [116], Copyright 2014 Royal Society of Chemistry. (c) Illustration of synthesis process of Co-MOL@GO. TEM image (d) and AFM analysis (e) of Co-MOL@GO, (f) Time-resolved absorption spectra of blank RuPS, RuPS with triethanolamine, RuPS with Co-MOL@GO and RuPS with Co-MOF in acetonitrile with the excitation wavelength of 450 nm; (g) Proposed mechanism of photoreduction of CO_2 over Co-MOL@GO. (c–g) Reprinted with permission from Ref. [70], Copyright 2021, Nature Publishing Group.

ferent substituent groups, resulting from the "electron acceptor" role of GR, which can facilitate the migration and prolong the lifetime of photoexcited electrons.

In addition to semiconductor materials, MOFs or 2D metal-organic layers (MOLs) are also integrated with GR to improve the charge separation and transport efficiency of composites. For example, GO as the precursor of GR has been used as a 2D template to synthesize ultrathin Co-MOLs NSs by Wang *et. al.* [70]. As shown in Fig. 7(c), Co^{2+} ions are firstly immobilized on 2D GO (Co@GO) in the mixture of ethanol and water by oil bath treatment. Then, the solvothermal method is used to prepare Co-MOL@GO with the addition of Co@GO and 5-(1H-1,2,4-triazol-1-yl)isophthalic acid. Fourier-transform infrared (FTIR) spectra and X-ray diffraction (XRD) analyses jointly demonstrate the successful graft of Co-MOLs on GO, which is substantially reduced to GR in solvothermal process. Transmission electron microscopy (TEM) image (Fig. 7(d)) portrays that Co-MOLs nanoflakes with size of 15–20 nm are uniformly distributed on GO sheets. In Fig. 7(e), atomic force microscopic (AFM) anlysis demonstrates that Co-MOLs are *ca.* 20 nm in diameter and *ca.* 1.5 nm in thickness. Using $Ru(phen)_3(PF6)_3$ (abbreviated as RuPS) as photosensitizer, a CO yield of 216.2 mmol g^{-1} with the selectivity of 95% is obtained over Co-MOL@GO after 12 h visible light irradiation, which is superior to that of Co-MOF. The comprehensive analyses of PL spectra (Fig. 7(f)), time-resolved absorption spectroscopy and *in situ* transient photovoltage (TPV) have been used to unveil the photocatalytic CO_2 reduction mechanism over Co-MOL@GO. In this system, GO as an efficient mediator provides conductive channels to boost electrons transfer from RuPS to Co-MOLs, which represent the active sites for CO_2 photoreduction (Fig. 7(g)). Furthermore, during the synthesis procedure, GO also acts as a template to decrease surface energy of ultrathin Co-MOLs and hence stabilize them.

In another example of using GR to fabricate 2D photocatalytic materials, ultrathin 2D Ni_2P NSs on functionalized single-layer graphene (FGR) have been fabricated by a facile and scalable route (Fig. 8(a)) [59]. Initially, solvothermal method is used to prepare ultrathin β-$Ni(OH)_2$ NSs with the aid of cetyltrimethylammonium bromide (CTAB). Then, positively charged β-$Ni(OH)_2$ NSs are hybridized with negatively charged sodium dodecyl sulfate (SDS)-FGR by electrostatic self-assembly process. Finally, the as-obtained $Ni(OH)_2$-FGR transforms to Ni_2P-FGR *via* a low-temperature phosphorization treatment. The comparative researches utilizing EGR and GO disclose that the introduction of FGR with oxygenated functional groups and large size is conducive to forming the interfacial bonding with Ni_2P NSs and decreasing the lattice strain during the phosphorization (Fig. 8(b)), thus maintaining the ultrathin morphology of Ni_2P NSs, which can be demonstrated by the scanning electron microscopy (SEM) and AFM images in Figs. 8(c) and (d). The visible light-driven H_2 yield of Ni_2P-FGR is superior to that of $Ni(OH)_2$-FGR and aggregated blank Ni_2P toward H_2 production with eosin Y (EY) as photosensitizer. In Figs. 8(e) and (f), compared with bare Ni_2P, the decreased PL intensity and enhanced current density of Ni_2P-FGR suggest that introducing FGR improves the charge transfer kinetics of Ni_2P-FGR composite. To sum up, in Ni_2P-FGR-EY system, the photoelectrons generated from EY are accepted and shuttled by electrically conductive FGR, during which the π-π interactions

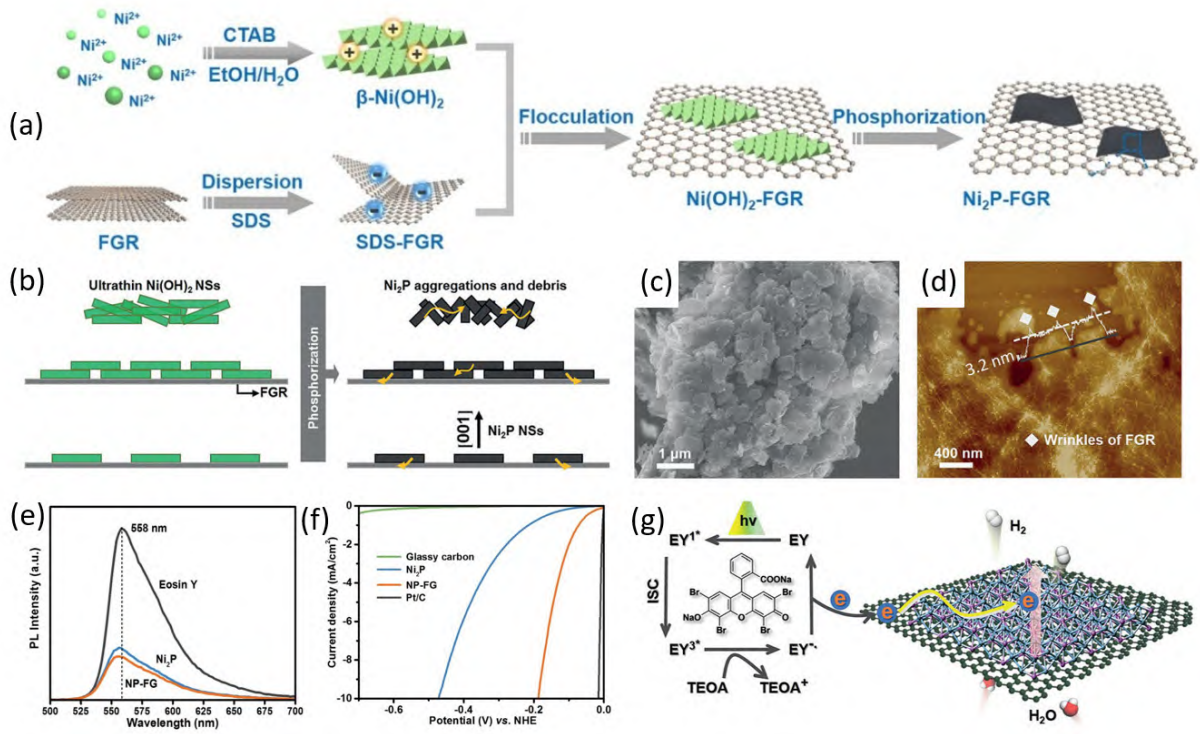

Fig. 8. (a) Diagram of synthesis process of Ni_2P-FGR; (b) Diagram of Ni_2P NSs synthesis utilizing FGR to reduce lattice strain during phosphating treatment; TEM image (c) and AFM analysis (d) of Ni_2P-FGR; PL spectra (e) and LSV curves (f) of Ni_2P and Ni_2P-FGR; (g) Mechanism of visible light-driven H_2 evolution over Ni_2P-FGR-EY. Reprinted with permission from Ref. [59], Copyright 2018, Wiley-VCH.

between FGR and EY facilitate the charge separation. The Ni_2P NSs with exposed (001) facet provide abundant active sites to promote H_2 evolution over Ni_2P-FGR (Fig. 8(g)). This work provides a useful guidance for using GR to reduce the lattice strain during phosphating treatment, which could be extended to the preparation of other ultrathin flake-like materials for varieties of energy and environmental applications.

Considering that irreversible aggregation of GR sheets during synthesis process may decrease the electronic conductivity of GR, constructing 3D GR-based gels involving aerogels and hydrogels, in which the interconnected porous structure provides multidimensional channels for electron migration has been considered to boost the separation efficiency of photoexcited electron-hole pairs. For instance, Xu *et al.* [52] have constructed RGA/AgBr/Ag composites by uniformly integrating AgBr and Ag on 3D rGO hydrogel scaffold, which can inhibit the aggregation of AgBr nanoparticles (NPs) and reduce Ag^+ cations to Ag NPs. In Fig. 9(a), the synthesis process of RGA/AgBr/Ag hybrid is described. Firstly, a low-temperature chemical reduction approach is used to prepare rGO hydrogel with $NaHSO_3$ as reductant, which could partially remove the hydrophilic oxygen-containing groups of GO to enhance the hydrophobicity and π-conjugated structure of rGO. The changed hydrophilic-hydrophobic balance results in the formation of integrated rGO hydrogel. Hereafter, the reduction of Ag^+ cations and decoration of AgBr NPs on CTAB modified rGO hydrogel are simultaneously realized. RGA/AgBr/Ag hydrogel possesses higher activity than that of blank AgBr toward photocatalytic disinfection of Escherichia coli (E. coli). The comprehensive analysis of electrochemical characterizations and PL spectra (Fig. 9(b)) demonstrates that RGA and Ag NPs as the electron transfer mediators significantly boost the charge carriers separation and migration. As depicted in Fig. 9(c), under visible light irradiation, photoelectrons generated from AgBr can be firstly captured by GR and then transferred to Ag NPs, or directly captured by AgBr-derived Ag NPs. The plasmonic Ag NPs can also be excited to generate hot electrons, which can be captured for taking part in the photocatalytic disinfection reaction and contributing to the photoactivity improvement of RGA/AgBr/Ag composite. This work provides an ingenious paradigm for the construction and environmental applications of 3D GR-based gels featuring interconnected porous structure and multiple electron migration channels.

Beyond that, SEG exfoliated in *N,N′*-dimethylformamide and EGR synthesized by a high-shear exfoliation procedure in liquid phase with decreased defect density and increased electrical conductivity have been employed to replace rGO as the photoinduced electron accepter to further boost the photocatalytic performance of GR-based composites [54,60,88]. Taking EGR as the example, Xu' group [60] has employed electrostatic self-assembly strategy to synthesize CdS-EGR and CdS-rGO hybrids, respectively, as represented in Fig. 10(a). For CdS-EGR, sodium dodecyl benzene sulfonate (SDBS) is used to modify EGR with additional hydrophilic groups, after that EGR becomes negatively charged and the solution processability of EGR improves, thereby facilitating the subsequent self-assembly processes. For CdS-rGO, CdS nanospheres (CdS NSPs) possessing positively charged surface are firstly assembled with negatively charged GO sheets. The following hydrothermal reaction is used to reduce GO in CdS-GO to rGO. The comparison of photocatalyzed H_2 production activity of CdS-EGR and CdS-rGO demonstrates that EGR with superior electrical conductivity can be used to replace rGO cocatalyst, thereby enhancing the photocatalytic performance of CdS NSPs. Transient photocurrent responses of as-synthesized samples in Fig. 10(b) suggest that the separation efficiency of photoinduced electrons and holes over CdS-EGR is higher than that over CdS and CdS-rGO.

As the superior conductivity of EGR demonstrated above, EGR has been introduced into the synthesis procedure of 3D rGO aerogel to improve the charge carrier mobility of composite aerogel [54]. As shown in Fig. 10(c), the calculated amount of EGR, GO and EY are sequentially mixed together by ultrasound treatment and stirring. The well-mixed EGR@GO-EY dispersion is subjected to hydrothermal treatment and the

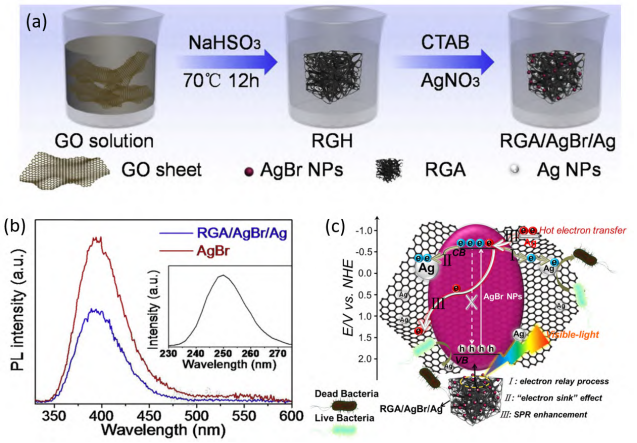

Fig. 9. (a) Diagram of preparation method of RGA/AgBr/Ag hybrid; (b) PL spectra of bare AgBr and RGA/AgBr/Ag composite; (c) Possible mechanism of photocatalytic *e.* coli cells inactivation over RGA/AgBr/Ag hybrid. Reprinted with permission from Ref. [52], Copyright 2019, Elsevier.

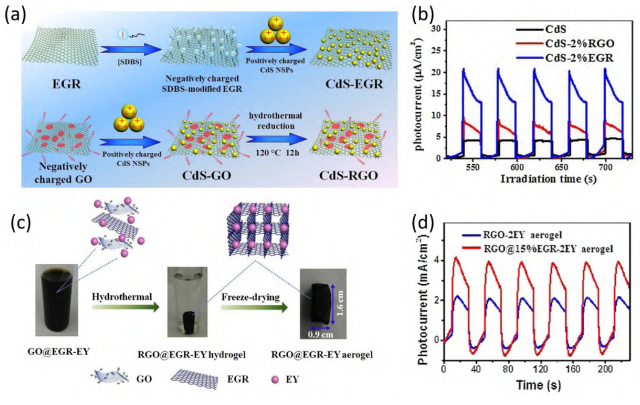

Fig. 10. (a) Illustration of synthesis process of CdS-EGR and CdS-rGO; (b Transient photocurrent responses of bare CdS, CdS-EGR and CdS-rGO composites. (a,b) Reprinted with permission from Ref. [60], Copyright 2018 Elsevier. (c) Diagram of synthesis method of rGO@EGR-EY aerogel; (d) Transient photocurrent responses of rGO-EY and rGO@EGR-EY aerogels. (c,d) Reprinted with permission from Ref. [54], Copyright 2018, Elsevier.

as-prepared rGO@EGR-EY hydrogel is treated by freeze-drying. During the synthesis, GO serving as the macromolecular surfactant is used to overcome the intrinsic shortcoming of low dispersity of EGR in solution and provide basic framework for the assembly of rGO@EGR-EY composite aerogels. As uncovered by transient photocurrent responses in Fig. 10(d), compared with rGO-EY, rGO@EGR-EY aerogel possesses higher separation efficiency of photoinduced charge carriers due to its enhanced electrical conductivity. Consequently, the photocatalytic Cr (VI) reduction rate of rGO@EGR-EY is higher than that of rGO-EY. These works open promising prospects for advancing the reasonable exploitation of electrically conductive SEG and EGR to construct highly active GR-based composites for enhanced photoredox applications.

In another aspect, although charge transfer kinetics is recognized as the most pivotal factor influencing the activity of GR-based photocatalysts, the design and exposure of catalytic active sites are also crucial for enhancing the performance of specific photocatalytic systems. For example, Xu and coworkers [58] have disclosed the double-edged sword role of GR on promoted electron migration versus active site regulation by constructing 3D TiO_2 nanotube arrays@rGO/MoS_2 ($TNTAs@rGO/MoS_2$) composite. The overall synthesis process for ternary $TNTAs@rGO/MoS_2$ hybrid is graphically depicted in Fig. 11(a). Firstly, a two-step anodization treatment is used to synthesize vertically aligned TNTAs. In the following, the GO is electrodeposited on TNTAs matrix by the cyclic voltammetry approach, while the GO is electrochemically reduced to rGO. The number of potential cycling controls the loading ratio and surface coverage of rGO. Finally, utilizing $(NH_4)_2MoS_4$ as precursor, MoS_2 is photodeposited on binary composite to construct $TNTAs@rGO/MoS_2$ (Fig. 11(b)), in which TNTAs with vectorial charge transfer paths are selected as the light absorber, electrodeposited rGO film acts as the charge mediator, and ultrafine MoS_2 serves as the catalytic sites for H_2 production. In Figs. 11(c) and (d), it is interesting to find that TNTAs@rGO possesses lower H_2 yield than that of TNTAs while the photocurrent density of TNTAs@rGO is higher than that of TNTAs, which is ascribed to the decreased catalytic sites for H_2 production over binary TNTAs@rGO as compared to bare TNTAs. After loading MoS_2 as efficient active sites, the H_2 evolution rate over $TNTAs@rGO/MoS_2$ is higher than that over TNTAs@rGO and $TNTAs/MoS_2$ composites, which ties in with the results of transient photocurrent responses. Above data manifest that

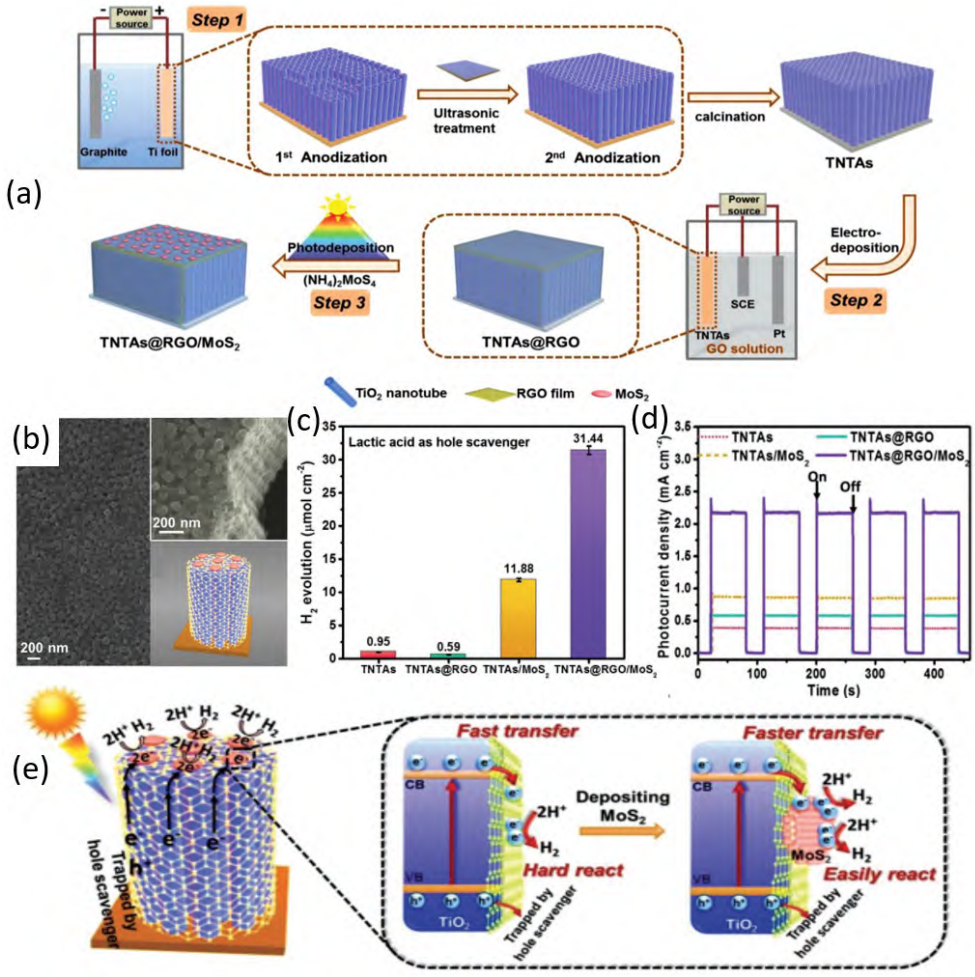

Fig. 11. (a) Diagram of preparation procedure of $TNTAs@rGO/MoS_2$; (b) SEM images of top and side section, along with the diagram of $TNTAs@rGO/MoS_2$; Photoactivity of H_2 evolution (c) and transient photocurrent responses (d) of as-prepared samples; (e) Diagram of photocatalytic mechanism of H_2 production over as-prepared catalysts. Reprinted with permission from Ref. [58], Copyright 2018, Wiley-VCH.

both charge separation/transfer efficiency and active sites design play important roles in enhancing the photoactivity of TNTAs@rGO/MoS_2 composite (Fig. 11(e)). This work reveals that the integrated optimization of catalyst design by tuning electron transfer pathways and exposing active sites for specific photocatalytic system needs to be considered when GR is utilized as cocatalyst to boost the activity of semiconductor-based catalysts.

3.2. *Improving adsorption capacity*

On account of its planar morphology, distinct surface properties, and high specific surface area, the fundamental role of GR in improving adsorption capacities of composite photocatalysts towards various reactants, such as CO_2, aromatic alcohols, and toxic pollutants *via* physical adsorption, electrostatic attraction, or chemical interaction has also been widely reported. The proper and efficient adsorption of reactant molecules and sacrificial reagents is conducive to the rapid participation of reactant molecules in surface reactions and rapid consumption of photoexcited charge carriers, resulting in the enhanced photoactivity of GR-based hybrids [39,115].

For instance, Xu *et al*. [48] have reported the ingenious assembly of a class of transition metal hydroxides, including $Ni(OH)_2$, $Fe(OH)_3$, $Cu(OH)_2$, and $Co(OH)_2$ on 2D GR sheets to serve as the highly-efficient cocatalyst ensemble for photocatalytic CO_2 reduction. As sketched in Fig. 12(a), transition metal hydroxides are synthesized on GR sheets by *in situ* heterogeneous nucleation and oriented crystal growth process in solution phase. When transition metal precursor is added into GO solution, transition metal cations (Ni^{2+}, Fe^{3+}, Cu^{2+} or Co^{2+}) are firmly adsorbed on the surface of negatively GO *via* the strong electrostatic interaction. Then, hexamethylenetetramine (HMTA) as a hydrolyzing agent slowly decomposes to produce OH^- ions, which subsequently react with transition metal cations to fabricate the dense nuclei of transition metal hydroxides on GO surface. Because the steric hindrance from nearby nuclei restrains the in-plane direction growth of transition metal hydroxides, the nuclei of transition metal hydroxide tend to form nanoflakes during thermal reflux process, while GO sheets are reduced to GR. As signified in Fig. 12(b), $Ni(OH)_2$ nanosheet arrays are homogeneously wrapped on the surface of GR sheets. With $[Ru(bpy)_3]Cl_2·6H_2O$ (abbreviated as Ru) as photosensitizer, whether in pure CO_2 or diluted CO_2, $Ni(OH)_2$-10%GR possesses excellent CO production rate and selectivity, which remarkably outperform that of bare $Ni(OH)_2$ and GR. Because $Ni(OH)_2$-GR exhibits optimal photoactivity among these transition metal hydroxide-GR, it is selected to study the underlying origin for activity improvement of these composites. As confirmed by N_2 adsorption-desorption isotherms in Fig. 12(c), $Ni(OH)_2$-10%GR exhibits an obviously higher Brunner-Emmet-Teller (BET) surface area compared with bare $Ni(OH)_2$ and $Ni(OH)_2$ NPs-10%GR hybrid, indicating that the introduction of GR endows composite cocatalysts with increased specific surface area. Increasing the surface area of $Ni(OH)_2$-10%GR can expose more active sites, promote the mass transport of reactants and products, thus leading to the enhanced photoactivity. In Figs. 12(d) and (e), CO_2 adsorption

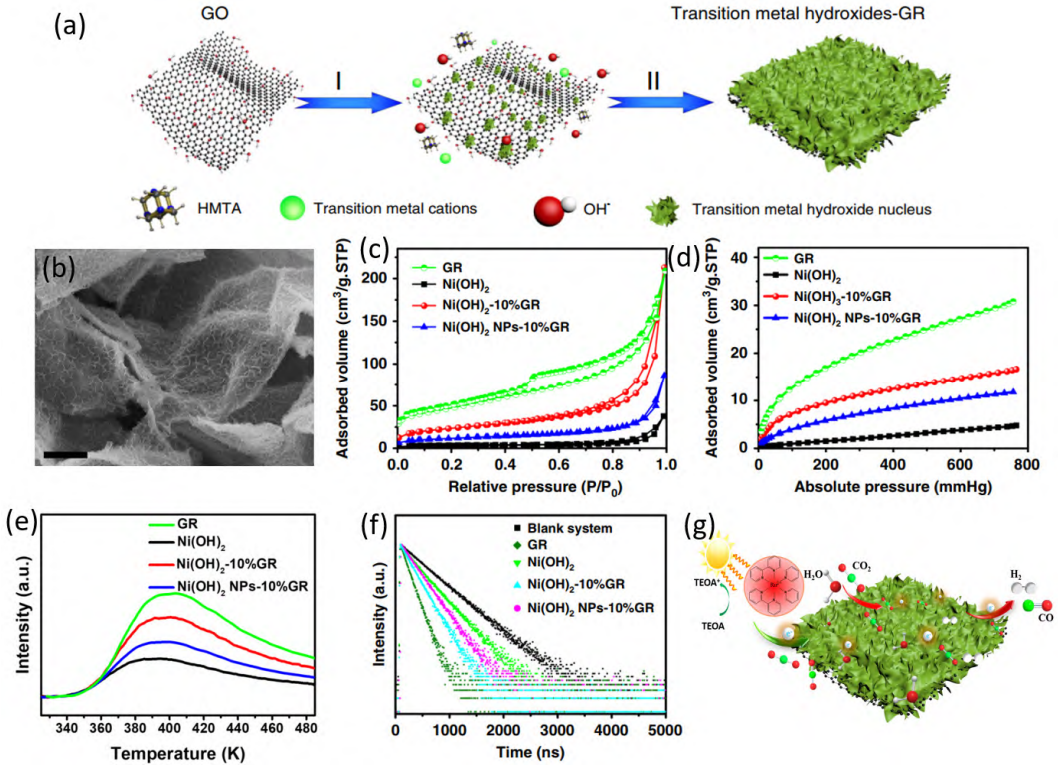

Fig. 12. (a) Diagram of fabrication method of transition metal hydroxides-GR composites; (b) SEM image of $Ni(OH)_2$-10%GR; N_2 adsorption-desorption isotherms (c), CO_2 adsorption isotherms (d), CO_2 TPD (e) and TRPL spectra (f) of as-prepared cocatalysts; (g) Probable mechanism of CO_2 photoreduction over $Ni(OH)_2$-10%GR. Reprinted with permission from Ref. [48], Copyright 2020, Nature Publishing Group.

isotherms and CO_2 temperature-programmed desorption (TPD) results synergistically demonstrate that the utilization of GR and the preparation of hierarchical nanosheet array structure significantly improve the CO_2 adsorption capacity of $Ni(OH)_2$-10%GR, which facilitates the enrichment and activation of CO_2 molecules, thus increasing the activity of $Ni(OH)_2$-10%GR for CO_2 photoreduction. Moreover, Figs. 12(f) and (g) elucidate that GR not only enhances the CO_2 adsorption capacity but also acts as the electron-conductive medium to boost the separation and migration of charge carriers in this system, thereby boosting the photoactivity over $Ni(OH)_2$-10%GR toward Ru-sensitized CO_2 reduction under visible light.

Moreover, Xu *et al*. [165] have reported that P25 NPs and GO mixed in the solvent of water and ethanol are treated by a simple hydrothermal method to synthesize rGO-P25, during which GO sheets are reduced to GR. The adsorption equilibrium in dark (Fig. 13(a)) demonstrates that the adsorption capacity of rGO-P25 is higher than that of blank P25, which contributes to the improved photoactivity toward liquid-phase methylene blue (MB) degradation. Furthermore, the adsorption kinetics studies have also been performed to evaluate the adsorption behavior of photocatalysts. For instance, rGO/$ZnFe_2O_4$ (RG/ZF) hybrids with different loading amount of rGO have been synthesized *via* chemical co-precipitation approach with $Zn(NO_3)_2{\cdot}6H_2O$ and $Fe(NO_3)_2{\cdot}9H_2O$ as precursors and NaOH as precipitant. As presented in Fig. 13(b), RG/ZF composites exhibit higher rhodamine B (RhB) adsorption capacity than that of blank $ZnFe_2O_4$ [166]. With the increase of mass ratio of rGO to $ZnFe_2O_4$, the adsorption capacity of RG/ZF increases, demonstrating the contribution of GR loading to the adsorption capacity improvement of RG/ZF hybrids. In Fig. 13(c), the adsorption results are well fitted with second-order kinetic model and the adsorption of RhB on RG/ZF composites belongs to chemisorption. The adsorption data also confirm that introducing rGO increases the adsorption rate of RG/ZF composites toward RhB.

Apart from 2D GR sheets, the construction of 3D gel featuring abundant porous structure is also beneficial to enhance the adsorption capacity of GR-based composites. For instance, Xu' group [84] has prepared 3D rGO/$Ti_3C_2T_x$ (RTiC) hydrogel by a one-step GO assisted self-convergence method. As shown in Fig. 14(a), $Ti_3C_2T_x$ colloid is firstly mixed with GO colloidal solution *via* continuous stirring. After that, the mixture was subjected to reaction at 70 °C with the addition of $NaHSO_3$ to form a monolithic RTiC hydrogel with interconnected porous network (Fig. 14(b)). For comparison, RTiC hydrogel has been dried at 60 °C to prepare RTiC powder, in which NSs are seriously stacked and the accessible active areas is smaller than that of RTiC hydrogel, as depicted in Figs. 14(c) and (d). In FTIR spectra of GO/$Ti_3C_2T_x$ and GO within 30 h (Figs. 14(e) and (f)), the characteristic peak of C–O for GO/$Ti_3C_2T_x$ gradually disappears while the peak of C–O for GO has almost no change, implying that GO is reduced to rGO in the synthesis process on account of the reduction ability of $Ti_3C_2T_x$. In Fig. 14(g), Raman spectra demonstrate that using $NaHSO_3$ as reducing agent can alleviate the oxidation of $Ti_3C_2T_x$, thus facilitating the utilization of superior electrical conductivity of $Ti_3C_2T_x$ for photocatalytic reactions. After immobilizing EY as photosensitizer on 3D RTiC hydrogel, the as-prepared RTiC/EY hydrogel possesses superior photoactivity toward Cr (VI) reduction and 4-nitroaniline (4-NA) conversion compared with RTiC/EY powder under visible light illumination. As observed in Fig. 14(h), RTiC/EY hydrogel exhibits higher adsorption capacity toward Cr (VI) and 4-NA than that of RTiC/EY powder, which is attributed to the decreased nanosheet aggregation and large specific surface area caused by the interconnected porous structure of RTiC/EY hydrogel. In addition to the enhanced adsorption capacity, the enhanced charge transfer efficiency of RTiC/EY hydrogel caused by its multidimensional electron transfer channels is also conducive to the photocatalytic performance improvement of RTiC/EY hydrogel.

3.3. Tuning light absorption range and intensity

Considering that light absorption is the forerunning step of photocatalysis, tuning the light absorption range and intensity of semiconductor materials by integrating GR with them is considered as an appealing strategy to improve the photocatalytic performance of GR-based hybrids. Especially for wide band gap semiconductors, using appropriate method to integrate GR with them is beneficial to expand their light absorption range from UV to visible light [140,167–169].

For example, Xu *et al*. [170] have utilized GO as the struc-

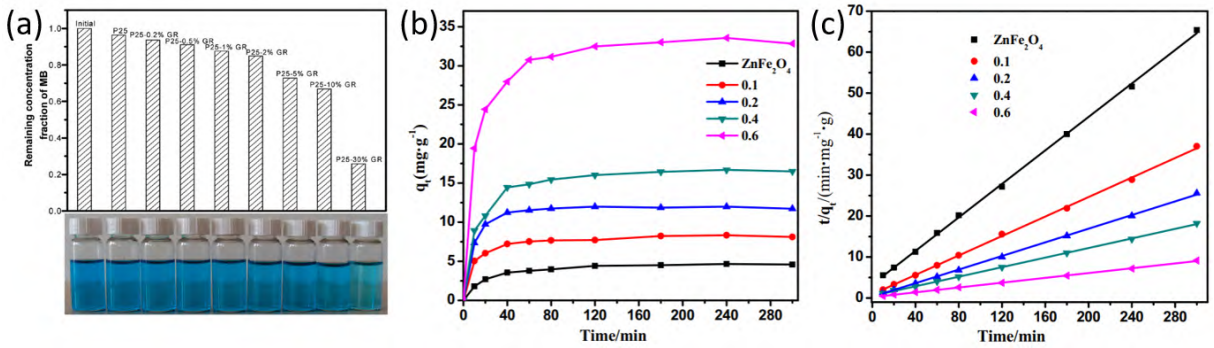

Fig. 13. (a) Remaining concentration of MB after reaching adsorption equilibrium over P25-GR composites and photos of corresponding MB solution of each catalyst. Reprinted with permission from Ref. [165], Copyright 2010 American Chemical Society. Adsorption kinetics (b) and adsorption mechanism (c) of $ZnFe_2O_4$ and RG/ZF composites. (b,c) Reprinted with permission from Ref. [166], Copyright 2015, Elsevier.

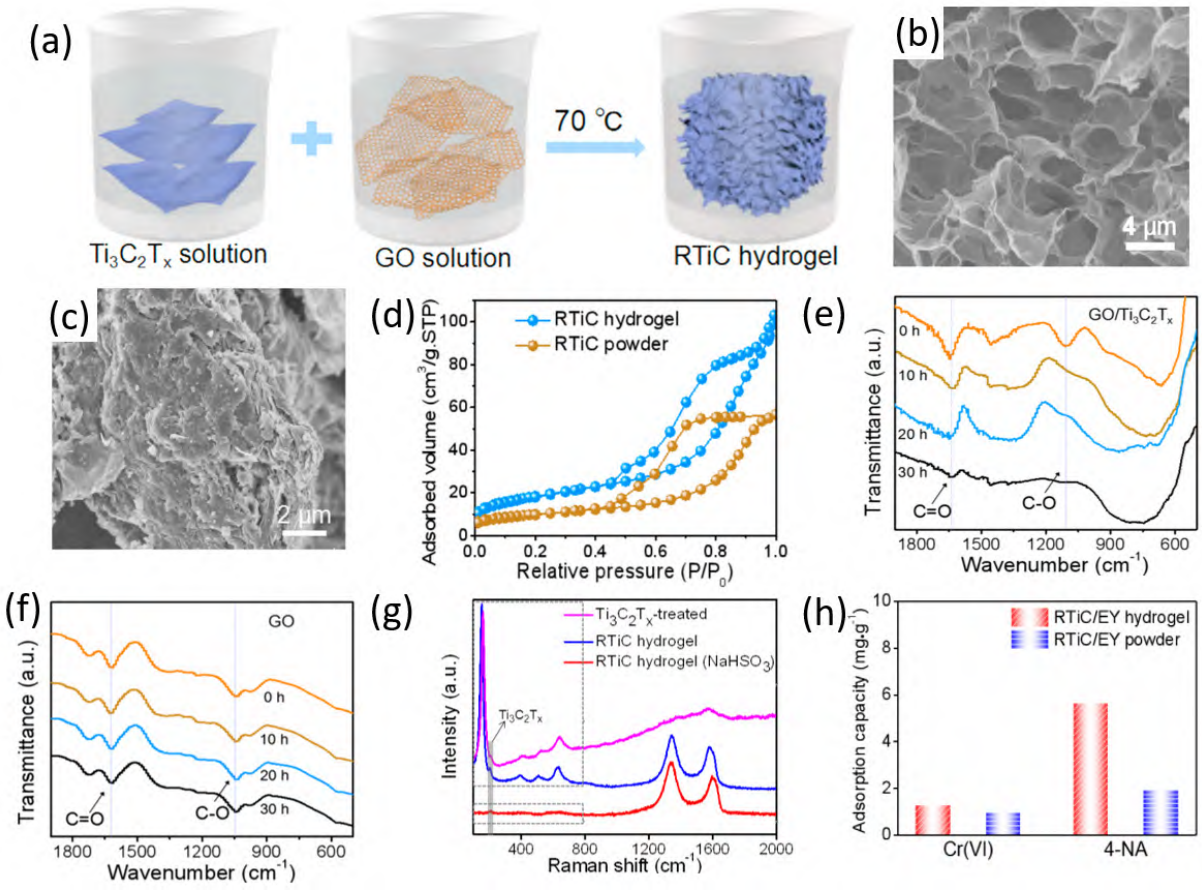

Fig. 14. (a) Diagram of synthesis process of RTiC hydrogel; SEM images of RTiC hydrogel (b) and RTiC powder (c); (d) N_2 adsorption-desorption isotherms of RTiC hydrogel and RTiC powder; FTIR spectra of GO/$Ti_3C_2T_x$ (e) and GO (f) in different reaction times; (g) Raman spectra of RTiC hydrogel, $Ti_3C_2T_x$ treated at 70 °C and RTiC hydrogel synthesized without $NaHSO_3$; (h) Adsorption capacity of RTiC hydrogel and RTiC powder toward Cr (VI) and 4-NA. Reprinted with permission from Ref. [84], Copyright 2019, American Chemical Society.

ture-directing macromolecular surfactant to fabricate rGO-ZnO composites, in which the light absorption range of ZnO can be broadened from UV to visible light. As displayed in Figs. 15(a)–(d), with the enhancement of GO amount during the preparation procedure, 1D ZnO nanorods gradually change to hexagonal ZnO nanotubes while GO is reduced to rGO. The contrast experiments with rGO as surfactant interpret that GO with surficial oxygen-containing groups plays a vital role in tailoring the morphology of ZnO. In addition, the mechanism of morphology changes of ZnO with the increase of GO content is described in Fig. 15(e). Initially, Zn^{2+} cations are adsorbed on the oxygenated functional groups of GO *via* electrostatic force. Under thermal conditions, HMTA decomposes to OH^- ions, which react with Zn^{2+} cations to promote the nucleation of ZnO on GO flat, resulting in the intimately connected interface of rGO-ZnO. Due to the interaction between Zn^{2+} cations and oxygenated groups on GO surface, the formation of (0001) crystal plane of wurtzite ZnO is suppressed and the flat-tip of ZnO rods is formed. When the addition amount of GO increases, the polar planes of ZnO are eroded, leading to the morphology transformation from ZnO rod to ZnO tube. Besides, electron spin resonance (EPR) and PL spectra prove that the oxygen-containing groups on GO can induce the generation of oxygen defects in ZnO lattice and the concentration of oxygen defects is affected by the amount of GO. Because the formation of oxygen defects introduces impurity levels above valence band (VB) of ZnO, the band gap of ZnO in rGO-ZnO composites is narrowing, which is in agreement with the broadened light absorption range of ZnO (Figs. 15(f) and (g)). Moreover, the narrowed band gap of ZnO is also affected by the strong interfacial interaction between ZnO and rGO. Arising from the generation of oxygen defects and tightly connected interface of rGO-ZnO, rGO-ZnO composites possess markedly improved Cr (VI) reduction activity under visible light illumination whereas blank ZnO only exhibits UV light-driven activity. This work emphasizes that GO as the precursor of GR can act as a surfactant to regulate the morphology and defect structure of as-fabricated rGO-semiconductor composites, which play a significant role in broadening the light absorption region and consequently optimizing the photocatalytic performance.

Taking rGO-P25 as another example, which is fabricated *via* a one-step hydrothermal reaction (Fig. 16(a)). The diffuse reflectance spectroscopy (DRS) (Fig. 16(b)) elucidates that introducing rGO into the matrix of P25 enhances the light absorption intensity and broadens the light absorption range of P25 to visible light region [171]. As manifested in FTIR spectra (Fig. 16(c)), the peaks located at 1600 and 1726 cm^{-1} are respectively ascribed to the skeletal vibration of GR and C–O

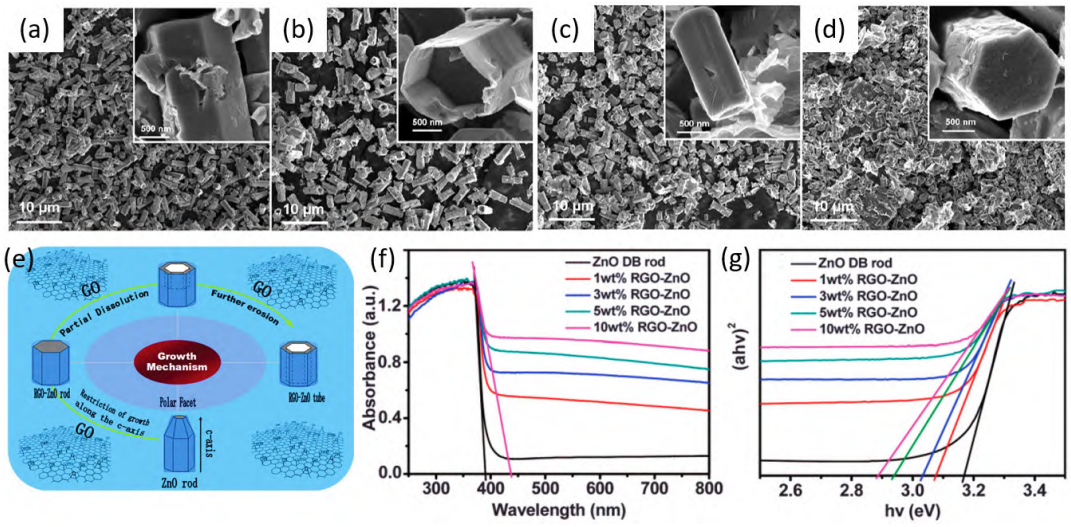

Fig. 15. SEM images of rGO-ZnO hybrids with different rGO weight ratios: (a) 1 wt%; (b) 3 wt%; (c) 5 wt%; and (d) 10 wt%. (e) Probable mechanism for the formation of rGO-ZnO; DRS (f) and Tauc plots (g) of ZnO and rGO-ZnO composites. Reprinted with permission from Ref. [170], Copyright 2014, Royal Society of Chemistry.

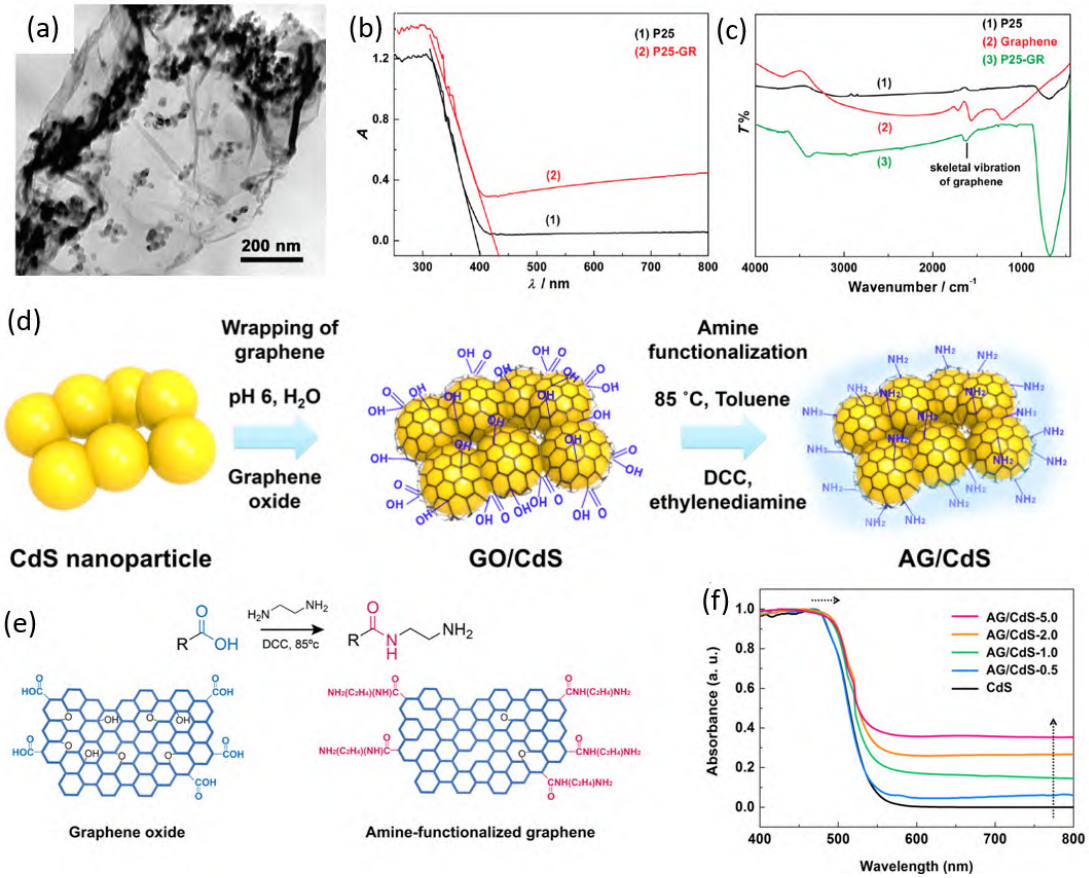

Fig. 16. (a) TEM image of P25-GR; (b) DRS of P25 and P25-GR; (c) FTIR spectra of P25, GR and P25-GR. (a–c) Reprinted with permission from Ref. [165], Copyright 2010 American Chemical Society. (d) Schematic of fabrication method of AG/CdS composite; (e) Diagram for the amine functionalization of GO; (f) DRS of CdS and AG/CdS composites. (d–f) Reprinted with permission from Ref. [172], Copyright 2017, American Chemical Society.

stretching of carboxyl groups, uncovering that hydrothermal treatment reduces substantial GO to GR. For P25, the absorption band located at 690 cm^{-1} is assigned to the vibration of Ti–O–Ti bond in TiO_2. Compared to blank P25, P25-GR exhibits a broad and shifted absorption peak at 798 cm^{-1}, which can be assigned to Ti–O–Ti and Ti–O–C vibrations. The generation of Ti–O–C bond in P25-rGO hybrid enables the narrowed band gap and extended light absorption range of P25, which boost the photoactivity enhancement of P25-GR hybrids for photodegradation of MB.

As for the visible light responsive semiconductors, such as CdS and $ZnIn_2S_4$, the loading of GR mainly improves the light absorption intensity of composite photocatalysts [116]. For instance, the amine-functionalized graphene/CdS (AG/CdS) composites synthesized by the combination of hydrothermal and electrostatic self-assembly methods are used for CO_2 photoreduction [172]. As shown in Fig. 16(d), CdS NPs synthesized by solvothermal treatment are firstly functionalized with 3-aminopropropyltriethoxysilane (APTES) to obtained positively charged surface of CdS NPs. Subsequently, positively charged CdS NPs are loaded on GO with negative charge by dint of electrostatic attraction. Finally, as shown in Fig. 16(e), an *N,N′*-dicyclohexylcarbodiimide coupling reaction is utilized to functionalize GO/CdS with amine. In Fig. 16(f), the light harvesting properties of blank CdS and AG/CdS hybrids are revealed by DRS. Bare CdS exhibits a strong absorption edge at *ca.* 550 nm, ascribing to the band gap of CdS. After introducing GR, the light absorption intensity of AG/CdS hybrids in the range of 550–800 nm gradually improves with the enhance of loading ratios of GR. In addition, as compared with CdS, the band gap of AG/CdS is slightly decreased, which may be correlated with the influence of doping π electrons from sp^2 carbon on GR. Notably, although the introduction of GR is beneficial to enhance the light absorption of GR-based composites, the content of GR needs to be reasonably regulated. Because the relatively high loading amount of GR in GR-based composites results in the light shielding effect, which decreases the optical transmission efficiency through the depth of reaction solution, thereby suppressing the photocatalytic activity [116].

3.4. Macromolecular photosensitizer

Besides, GR can not only act as the cocatalyst to improve photoactivity, but also behave as the macromolecular photosensitizer to generate electrons for photocatalytic reactions under visible light illumination, which enriches the multifunctional facets of GR in GR-based photocatalytic systems [41,44–47,173,174]. In 2012, Xu' group [46] has experimentally demonstrated the photosensitizer role of GR by constructing rGO-ZnS composites for visible light-driven oxidation of alcohols and alkenes. A two-step route has been used to synthesize rGO-ZnS composites. (1) ZnS is deposited on GO by stirring GO aqueous solution with $ZnCl_2$ and Na_2S at room temperature; (2) Hydrothermal treatment is used to reduce GO to GR and promote the interfacial interaction between GR and ZnS. As depicted in DRS spectra (Fig. 17(a)), the introduction of rGO cannot change the absorption edge of ZnS to the visible light region, indicating that ZnS in rGO-ZnS hybrids cannot be band gap-photoexcited by visible light. However, rGO-ZnS hybrids possess visible light-driven activity toward selective conversion of benzyl alcohol while ZnS exhibits very poor activity and rGO do not exhibit activity. The correlation between structure and photoactivity, along with the mechanism study utilizing various radical scavengers indicate that the GR in rGO-ZnS serves as the macromolecular photosensitizer to generate electrons under visible light, which can migrate from GR to conduction band (CB) of ZnS to trigger photocatalytic reactions.

In another example, wide band gap $Ca_2Nb_3O_{10}$ monolayer NSs, which are synthesized by the proton exchange and exfoliation treatment of $KCa_2Nb_3O_{10}$ (KCNO) have been incorporated with rGO as photosensitizer (CNO_{MS}/rGO) through a hydrothermal route to catalyze the H_2 evolution and tetracycline hydrochloride degradation reactions under visible light illumination (Fig. 17(b)). Recently, the advances of theoretical calculations provide powerful means to investigate the electron structures, electron transfer manner, species adsorption of GR-based hybrids, along with the kinetic energy barriers and rate-determining step of photocatalytic reactions, which plays

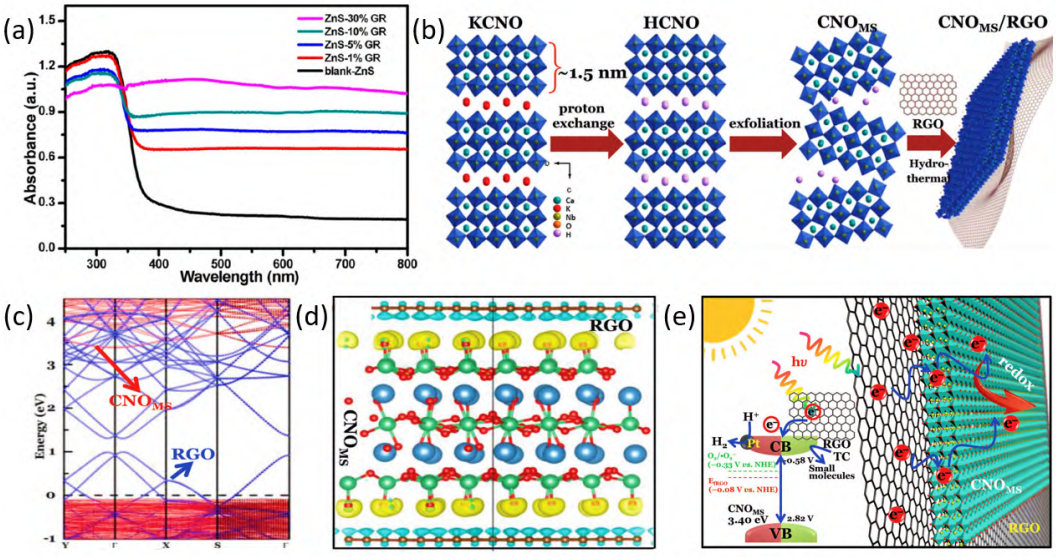

Fig. 17. (a) DRS of ZnS and ZnS-GR composites with diverse loading amount of GR. Reprinted with permission from Ref. [46], Copyright 2012 American Chemical Society. (b) Diagram of preparation procedure of CNO_{MS}/rGO; Band structure (c) and 3D charge density difference (d) of CNO_{MS}/rGO hybrids; (e) Diagram of photocatalytic mechanism of H_2 production over CNO_{MS}/rGO. (b–e) Reprinted with permission from Ref. [44], Copyright 2018, Wiley-VCH.

important roles in uncovering the catalytic mechanism at atomic level [135,175]. In this work, the electron transfer manner between photosensitizer rGO and CNO_{MS} ingredient in composite photocatalysts has been studied by density functional theory (DFT) calculations. As shown in Fig. 17(c), rGO exhibits p-type band structure and the band gap of CNO_{MS} is calculated as 3.4 eV, which is nearly in line with DRS result. The conduction bands and valence bands of CNO_{MS} are primarily occupied by Nb 4*d* and O 2*p*, respectively. In Fig. 17(d), the charge density difference (CDD, Δρ) is calculated to investigate the interfacial electron transfer between CNO_{MS} and rGO. In CNO_{MS}/rGO composites, the charge density of rGO is dissipative, which is opposite to that of CNO_{MS}, confirming the interfacial charge transfer from rGO to CNO_{MS} (Fig. 17(e)). In addition, the terminated oxygen atoms of CNO_{MS} possess strong electronegativity, which is conducive to accepting electrons generated from rGO.

In a following work, the ZnO NPs are *in situ* synthesized on GR sheets *via* a wet chemistry method to endow the closely interfacial combination between ZnO and GR for promoting the charge transport. The rGO-ZnO hybrids also possess visible light-driven activity for metal ions reduction, further revealing the photosensitizer role of GR [47]. Particularly, three fundamental tenets for exactly exploring the photosensitizer role of GR in GR-semiconductor-based catalysts have been proposed. (1) The semiconductor in GR-semiconductor hybrids cannot be visible light responsive; (2) The suitable interfacial connection between GR and semiconductor needs to be realized; (3) The proper probe reactions need to be selected to escape the self-induced photosensitization and effectively use the photoelectrons generated from GR under visible light illumination.

As shown in Fig. 18(a), for the purpose of improving the photosensitive efficiency of GR, Xu's group [41] has optimized the synthesis method for abovementioned rGO-ZnO composites by applying oxidation treatment to synthesize GO with smaller size (NanoGO) as the precursor of rGO, of which the density of oxygen-containing groups increases. In Figs. 18(b) and (c), upon visible light illumination, the activity of ZnO-NanorGO is remarkedly higher than that of ZnO-rGO toward Cr (VI) reduction. Controlled experiments uncover that the remaining content of oxygen-containing groups on rGO markedly influences the photosensitive efficiency of rGO. As revealed by theoretical calculations (Figs. 18(d) and (e)), when the amount of oxygen-containing functional groups increases, the band gap of GR will widen with the upshift of its CB. Therefore, the reduction capacity of photoelectrons generated from the photosensitization of GR enhances, leading to the improved photosensitive efficiency of GR. In addition, it is worth noting that the photosensitization efficiency of GR is still unsatisfactory, which can be improved by doping heteroatoms, adjusting the size and surface properties of GR. The types of photocatalytic reactions can also be further extended to CO_2 reduction and N_2 fixation.

4. Conclusions and future perspectives

In this review, we started with the introduction of optimization strategies of GR-based hybrids. Then, oriented by the fundamental roles of GR in photoredox catalysis, we outlined the

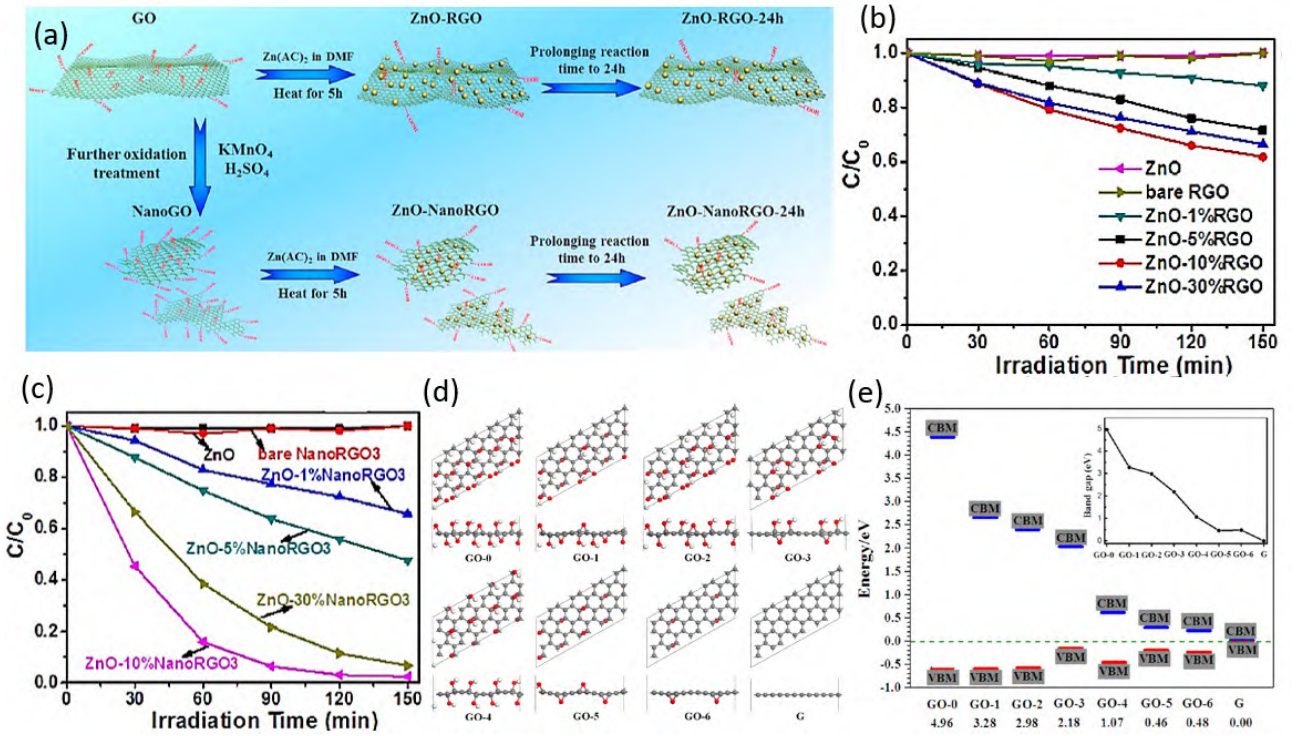

Fig. 18. (a) Illustration of synthesis procedure of ZnO-rGO and ZnO-NanorGO; (b) Photoactivity over bare ZnO and ZnO-rGO hybrids toward Cr (VI) reduction; (c) Photoactivity over bare ZnO and ZnO-NanorGO hybrids toward Cr (VI) reduction; (d) The calculated electronic properties of rGO with various number of oxygen-containing groups; (e) VBM and CBM of GO with different ratios of –O– and –OH groups. Reprinted with permission from Ref. [41], Copyright 2016, American Chemical Society.

commonly used methods, such as hydrothermal/solvothermal synthesis, electrochemical deposition and electrostatic self-assembly approach for the preparation of GR-based composites. Obviously, choosing suitable synthesis method and optimizing synthesis conditions play a crucial role in tailoring the morphology, size, defect structure, surface properties and interfacial parameters of GR-based composites, which significantly influence the performance of composite photocatalysts. To date, although myriads of advances have been achieved in this booming research field, there is still much space for researchers to exploit optimization strategy for the construction of GR-based composites with artful architectures and ideal performance.

In view of the current fact of the obvious incongruity between photoconversion efficiency of as-prepared GR-based hybrids and requirements of practical applications, constructing more efficient GR-based photocatalysts by well-designed synthesis procedure needs to be rationally considered. In this regard, the optimization of individual ingredients in the composites and harmonious combination of each component are both essential to take full advantage of basic multifarious roles of GR in photocatalysis to improve photocatalytic efficiency. It is worth emphasizing that the design and synthesis of highly efficient of GR-based photocatalysts is not an issue of only considering how to use the specific role of GR, but a synergistic integration of each function of individual component in the GR-based composite photocatalysts toward achieving the collectively optimal photocatalytic performance.

On the one hand, given that the properties of GR, such as layer number, size, defect, edge structure and surface functional groups, significantly influence the photocatalytic performance of GR-based hybrids, the controlled synthesis of GR and precise regulation of GR properties are very necessary, which can be adjusted from the following aspects. (1) GO prepared by the modified Hummers' method is the most commonly used precursor of GR, but its properties are usually inhomogeneous. Thus, it is required to optimize the synthesis method to produce uniform GO while avoiding the environmental pollution and experimental safety hazard caused by the massive utilization of strong acids and oxidants during the synthesis process. (2) In the design and synthesis of GR-based hybrids, the control of lateral dimension of GR is always neglected, which affects the synthesis and photoactivity of GR-based hybrids. In this context, the reasonable pre-/post-treatment of GR or its precursors, such as oxidation, functionalization, acid treatment needs to be further explored to realize the layer dimension-dependent synthesis of GR-based hybrids, thus boosting the photoactivity improvement. (3) Since the work function, thermal conductivity, electrical conductivity and hydrophilia of GR, Schottky barrier in GR-based hybrids, as well as interaction between GR and other ingredients are closely related to the layer number of GR, avoiding the aggregation of GR caused by van der Waals force between GR layers needs to be taken into account. Nowadays, apart from using ultrasonic treatment to alleviate the aggregation of GR, the development of simple and versatile layer-by-layer (LbL) self-assembly technology can simultaneously avoid GR stacking and accurately control the GR layer numbers, thereby realizing the layer-dependent synthesis of GR-based hybrids. Apart from the controllable synthesis of GR, the delicate regulation of properties (e.g., morphology, size and exposed crystal face) of other components, especially in ex situ synthesis, is also beneficial to the photoactivity improvement.

On the other hand, rationally tuning the interfacial parameters of GR-based hybrids, such as interfacial contact, interfacial composition and band bending alignment, would be able to promote the charge transport across the interfacial domain between GR and other components, thus increasing the overall photoactivity of GR-based composites. Moreover, given that GR generally plays multiple roles, which may affect each other in the photocatalytic system, the system-level harmonious integration of individual components needs to be taken into account when designing the specific photocatalysts.

And then, the exploration and optimization of novel approaches for large-scale synthesis of high-quality GR and GR-based composites are still highly desirable in future research. The underlying mechanism why GR can be used to tune the properties, such as morphology, size and defect structure of other components in GR-based composites needs in-depth investigations from the view of both thermodynamics and kinetics. In addition, although one of the key roles of GR is to boost photoelectrons migration, the investigations on working mechanism of GR accepting and transferring electrons in photocatalytic systems are still far from maturity. In this regard, the rapid developments of experimental technique, such as surface photovoltage microscopy (SPVM), electrostatic force microscopy (EFM), transient absorption microscopy (TAM), which could directly detect the spatial distribution and transfer direction of photoexcited charges, provide technical support for the study of charge separation and transfer kinetics of GR-based hybrids in high spatial and temporal resolution. Moreover, *in situ* characterizations (e.g., *in situ* FTIR, *in situ* environment transmission electron microscopy, *in situ* XPS and *in situ* X-ray absorption spectra) and theoretical simulations could provide us with numerous opportunities to advance our insight into the growth mechanism of photoactive materials on the platform of GR, microscopic charge transfer path and dynamics on GR, as well as the real-time conversion pathways of reactant molecules and reaction intermediates, which could in turn provide targeted guidance to continuous advancement of efficient design, fabrication and applications of GR-based composite photocatalysts in diverse fields.

References

[1] K. S. Novoselov, A. K. Geim, S. V. Morozov, D. Jiang, Y. Zhang, S. V. Dubonos, I. V. Grigorieva, A. A. Firsov, *Science*, **2004**, 306, 666–669.
[2] B. Weng, Y.-J. Xu, *ACS Appl. Mater. Interfaces*, **2015**, 7, 27948–27958.
[3] M.-Q. Yang, C. Han, Y.-J. Xu, *J. Phys. Chem. C*, **2015**, 119, 27234–27246.
[4] C. Han, Z. Chen, N. Zhang, J. C. Colmenares, Y.-J. Xu, *Adv. Funct. Mater.*, **2015**, 25, 221–229.
[5] Y. Zhang, N. Zhang, Z.-R. Tang, Y.-J. Xu, *J. Phys. Chem. C*, **2014**, 118,

Graphical Abstract

Chin. J. Catal., 2022, 43: 708–730 doi: 10.1016/S1872-2067(21)63871-8

Multifunctional graphene-based composite photocatalysts oriented by multifaced roles of graphene in photocatalysis

Yue-Hua Li, Zi-Rong Tang *, Yi-Jun Xu *
Fuzhou Uiversity

This review overviews optimizing strategies and synthesis of graphene-based composite photocatalysts oriented by the fundamental manifold roles of graphene in photocatalysis and proposes the key challenges and future perspectives for further investigations of graphene-based photocatalysts.

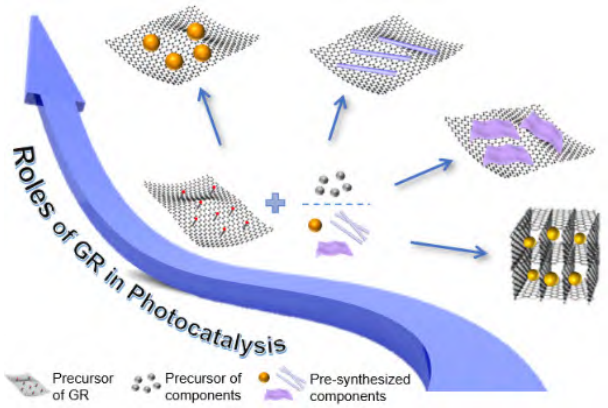

5299–5308.
[6] X. Guo, C. Hao, G. Jin, H.-Y. Zhu, X.-Y. Guo, *Angew. Chem. Int. Ed.*, **2014**, 53, 1973–1977.
[7] S. K. Bhunia, N. R. Jana, *ACS Appl. Mater. Interfaces*, **2014**, 6, 20085–20092.
[8] M. Zhu, P. Chen, M. Liu, *ACS Nano*, **2011**, 5, 4529–4536.
[9] N. Sadeghi, S. Sharifnia, T.-O. Do, *J. Mater. Chem. A*, **2018**, 6, 18031–18035.
[10] Z. Wang, J. Huang, J. Mao, Q. Guo, Z. Chen, Y. Lai, *J. Mater. Chem. A*, **2020**, 8, 2934–2961.
[11] M. Zhu, Y. Dong, B. Xiao, Y. Du, P. Yang, X. Wang, *J. Mater. Chem.*, **2012**, 22, 23773–23779.
[12] J. Cai, J.-Y. Lu, Q.-Y. Chen, L.-L. Qu, Y.-Q. Lu, G.-F. Gao, *New J. Chem.*, **2017**, 41, 3882–3886.
[13] G. Xie, K. Zhang, B. Guo, Q. Liu, L. Fang, J. R. Gong, *Adv. Mater.*, **2013**, 25, 3820–3839.
[14] P. Zhang, T. Song, T. Wang, H. Zeng, *Appl. Catal. B*, **2018**, 225, 172–179.
[15] D. Mateo, I. Esteve-Adell, J. Albero, J. F. S. Royo, A. Primo, H. Garcia, *Nat. Commun.*, **2016**, 7, 11819.
[16] S. Chen, T. Hisatomi, G. Ma, Z. Wang, Z. Pan, T. Takata, K. Domen, *Chin. J. Catal.*, **2019**, 40, 1668–1672.
[17] F. He, A. Meng, B. Cheng, W. Ho, J. Yu, *Chin. J. Catal.*, **2020**, 41, 9–20.
[18] S.-H. Li, R. Wang, Z.-R. Tang, Y.-J. Xu, *Catal. Today*, **2019**, 335, 160–165.
[19] X. Xie, N. Zhang, Z.-R. Tang, Y.-J. Xu, *Chem. Sci.*, **2018**, 9, 8876–8882.
[20] R. Wang, K.-Q. Lu, F. Zhang, Z.-R. Tang, Y.-J. Xu, *Appl. Catal. B*, **2018**, 233, 11–18.
[21] L. Zhu, S. Ye, A. Ali, K. Ulla, K. Youn Cho, W.-C. Oh, *Chin. J. Catal.*, **2015**, 36, 603–611.
[22] B. Yuan, J. Wei, T. Hu, H. Yao, Z. Jiang, Z. Fang, Z. Chu, *Chin. J. Catal.*, **2015**, 36, 1009–1016.
[23] R. Zhang, W. Wan, D. Li, F. Dong, Y. Zhou, *Chin. J. Catal.*, **2017**, 38, 313–320.
[24] Y. Wu, L. Zhang, Y. Zhou, L. Zhang, Y. Li, Q. Liu, J. Hu, J. Yang, *Chin. J. Catal.*, **2019**, 40, 691–702.
[25] C.-Y. Zou, S.-Q. Liu, Z. Shen, Y. Zhang, N.-S. Jiang, W.-C. Ji, *Chin. J. Catal.*, **2017**, 38, 20–28.
[26] L. Yin, M. Zhao, H. Hu, J. Ye, D. Wang, *Chin. J. Catal.*, **2017**, 38, 1307–1314.
[27] L. Pei, Y. Yuan, W. Bai, T. Li, H. Zhu, Z. Ma, J. Zhong, S. Yan, Z. Zou, *ACS Catal.*, **2020**, 10, 15083–15091.
[28] C. Bie, B. Zhu, F. Xu, L. Zhang, J. Yu, *Adv. Mater.*, **2019**, 31, 1902868.
[29] J. O. Olowoyo, U. Saini, M. Kumar, H. Valdés, H. Singh, M. O. Omorogie, J. O. Babalola, A. V. Vorontsov, U. Kumar, P. G. Smirniotis, *J. CO_2 Util.*, **2020**, 42, 101300.
[30] S. Wang, M. Xu, T. Peng, C. Zhang, T. Li, I. Hussain, J. Wang, B. Tan, *Nat. Commun.*, **2019**, 10, 676.
[31] N. Zhang, Y. Zhang, M.-Q. Yang, Y.-J. Xu, *Curr. Org. Chem.*, **2013**, 17, 2503–2515.
[32] L. Yuan, Q. Yu, Y. Zhang, Y.-J. Xu, *RSC Adv.*, **2014**, 4, 15264–15270.
[33] Z. Li, Y. Pi, D. Xu, Y. Li, W. Peng, G. Zhang, F. Zhang, X. Fan, *Appl. Catal. B*, **2017**, 213, 1–8.
[34] Y. Pan, S. Wang, C. W. Kee, E. Dubuisson, Y. Yang, K. P. Loh, C.-H. Tan, *Green Chem.*, **2011**, 13, 3341–3344.
[35] A. K. Geim, *Science*, **2009**, 324, 1530–1534.
[36] K. S. Novoselov, V. I. Fal'ko, L. Colombo, P. R. Gellert, M. G. Schwab, K. Kim, *Nature*, **2012**, 490, 192–200.
[37] A. A. Balandin, S. Ghosh, W. Bao, I. Calizo, D. Teweldebrhan, F. Miao, C. N. Lau, *Nano Lett.*, **2008**, 8, 902–907.
[38] M. D. Stoller, S. Park, Y. Zhu, J. An, R. S. Ruoff, *Nano Lett.*, **2008**, 8, 3498–3502.
[39] N. Zhang, M.-Q. Yang, S. Liu, Y. Sun, Y.-J. Xu, *Chem. Rev.*, **2015**, 115, 10307–10377.
[40] M.-Q. Yang, N. Zhang, M. Pagliaro, Y.-J. Xu, *Chem. Soc. Rev.*, **2014**, 43, 8240–8254.
[41] K.-Q. Lu, N. Zhang, C. Han, F. Li, Z. Chen, Y.-J. Xu, *J. Phys. Chem. C*, **2016**, 120, 27091–27103.
[42] B. Bajorowicz, J. Reszczyńska, W. Lisowski, T. Klimczuk, M. Winiarski, M. Słoma, A. Zaleska-Medynska, *RSC Adv.*, **2015**, 5, 91315–91325.
[43] R.-X. Wang, Q. Zhu, W.-S. Wang, C.-M. Fan, A.-W. Xu, *New J. Chem.*, **2015**, 39, 4407–4413.
[44] D. Li, H. Zhao, L. Li, B. Mao, M. Chen, H. Shen, W. Shi, D. Jiang, Y. Lei, *Adv. Funct. Mater.*, **2018**, 28, 1806284.
[45] Y. Lu, B. Ma, Y. Yang, E. Huang, Z. Ge, T. Zhang, S. Zhang, L. Li, N. Guan, Y. Ma, Y. Chen, *Nano Res.*, **2017**, 10, 1662–1672.
[46] Y. Zhang, N. Zhang, Z.-R. Tang, Y.-J. Xu, *ACS Nano*, **2012**, 6,

9777–9789.
[47] M.-Q. Yang, Y.-J. Xu, *J. Phys. Chem. C*, **2013**, 117, 21724–21734.
[48] K.-Q. Lu, Y.-H. Li, F. Zhang, M.-Y. Qi, X. Chen, Z.-R. Tang, Y. M. A. Yamada, M. Anpo, M. Conte, Y.-J. Xu, *Nat. Commun.*, **2020**, 11, 5181.
[49] X. Huang, X. Qi, F. Boey, H. Zhang, *Chem. Soc. Rev.*, **2012**, 41, 666–686.
[50] Q. Xiang, J. Yu, M. Jaroniec, *Chem. Soc. Rev.*, **2012**, 41, 782–796.
[51] X. Li, J. Yu, S. Wageh, A. A. Al-Ghamdi, J. Xie, *Small*, **2016**, 12, 6640–6696.
[52] X. Xin, S.-H. Li, N. Zhang, Z.-R. Tang, Y.-J. Xu, *Appl. Catal. B*, **2019**, 245, 343–350.
[53] K.-Q. Lu, X. Xin, N. Zhang, Z.-R. Tang, Y.-J. Xu, *J. Mater. Chem. A*, **2018**, 6, 4590–4604.
[54] K.-Q. Lu, L. Yuan, X. Xin, Y.-J. Xu, *Appl. Catal. B*, **2018**, 226, 16–22.
[55] C. Han, N. Zhang, Y.-J. Xu, *Nano Today*, **2016**, 11, 351–372.
[56] Q. Quan, X. Lin, N. Zhang, Y.-J. Xu, *Nanoscale*, **2017**, 9, 2398–2416.
[57] J. Chen, J. Shi, X. Wang, H. Cui, M. Fu, *Chin. J. Catal.*, **2013**, 34, 621–640.
[58] Q. Quan, S. Xie, B. Weng, Y. Wang, Y.-J. Xu, *Small*, **2018**, 14, 1704531.
[59] S.-H. Li, N. Zhang, X. Xie, R. Luque, Y.-J. Xu, *Angew. Chem. Int. Ed.*, **2018**, 57, 13082–13085.
[60] K.-Q. Lu, Y. Chen, X. Xin, Y.-J. Xu, *Appl. Catal. B*, **2018**, 224, 424–432.
[61] Y. Wu, P. Wang, X. Zhu, Q. Zhang, Z. Wang, Y. Liu, G. Zou, Y. Dai, M.-H. Whangbo, B. Huang, *Adv. Mater.*, **2018**, 30, 1704342.
[62] Z. Pan, G. Zhang, X. Wang, *Angew. Chem. Int. Ed.*, **2019**, 58, 7102–7106.
[63] J. Zhang, Y. Li, X. Zhao, H. Zhang, L. Wang, H. Chen, S. Wang, X. Xu, L. Shi, L.-C. Zhang, J.-P. Veder, S. Zhao, G. Nealon, M. Wu, S. Wang, H. Sun, *ACS Nano*, **2020**, 14, 17505–17514.
[64] A. Iwase, S. Yoshino, T. Takayama, Y. H. Ng, R. Amal, A. Kudo, *J. Am. Chem. Soc.*, **2016**, 138, 10260–10264.
[65] Y.-F. Xu, M.-Z. Yang, B.-X. Chen, X.-D. Wang, H.-Y. Chen, D.-B. Kuang, C.-Y. Su, *J. Am. Chem. Soc.*, **2017**, 139, 5660–5663.
[66] X. Qiao, Q. Li, R. N. Schaugaard, B. W. Noffke, Y. Liu, D. Li, L. Liu, K. Raghavachari, L.-S. Li, *J. Am. Chem. Soc.*, **2017**, 139, 3934–3937.
[67] Y. Jiang, J.-F. Liao, H.-Y. Chen, H.-H. Zhang, J.-Y. Li, X.-D. Wang, D.-B. Kuang, *Chem*, **2020**, 6, 766–780.
[68] Y.-F. Mu, W. Zhang, G.-X. Dong, K. Su, M. Zhang, T.-B. Lu, *Small*, **2020**, 16, 2002140.
[69] X. Wang, K. Li, J. He, J. Yang, F. Dong, W. Mai, M. Zhu, *Nano Energy*, **2020**, 78, 105388.
[70] J.-W. Wang, L.-Z. Qiao, H.-D. Nie, H.-H. Huang, Y. Li, S. Yao, M. Liu, Z.-M. Zhang, Z.-H. Kang, T.-B. Lu, *Nat. Commun.*, **2021**, 12, 813.
[71] C. Gao, S. Chen, Y. Wang, J. Wang, X. Zheng, J. Zhu, L. Song, W. Zhang, Y. Xiong, *Adv. Mater.*, **2018**, 30, 1704624.
[72] Z. Yang, X. Xu, X. Liang, C. Lei, Y. Wei, P. He, B. Lv, H. Ma, Z. Lei, *Appl. Catal. B*, **2016**, 198, 112–123.
[73] Z. Li, Y. Pi, D. Xu, Y. Li, W. Peng, G. Zhang, F. Zhang, X. Fan, *Appl. Catal. B*, **2017**, 213, 1–8.
[74] X. Zhang, G. Kumari, J. Heo, P. K. Jain, *Nat. Commun.*, **2018**, 9, 3056.
[75] J.-Y. Li, X. Xin, Y.-H. Li, F. Zhang, M. Anpo, Y.-J. Xu, *Res. Chem. Intermed.*, **2019**, 45, 5935–5946.
[76] M. Yusuf, S. A. Hira, H. Lim, S. Song, S. Park, K. H. Park, *J. Mater. Chem. A*, **2021**, 9, 9018–9027.
[77] M. Wang, L. Cai, Y. Wang, F. Zhou, K. Xu, X. Tao, Y. Chai, *J. Am. Chem. Soc.*, **2017**, 139, 4144–4151.
[78] R. He, Z. Lou, J. Gui, B. Tang, D. Xu, *Appl. Surf. Sci.*, **2020**, 504, 144370.
[79] P. Chamoli, R. K. Shukla, A. N. Bezbaruah, K. K. Kar, K. K. Raina, *Appl. Surf. Sci.*, **2021**, 555, 149663.
[80] R. Santhosh Kumar, K. Govindan, S. Ramakrishnan, A. R. Kim, J.-S. Kim, D. J. Yoo, *Appl. Surf. Sci.*, **2021**, 556, 149765.
[81] L. Zhang, X. He, X. Xu, C. Liu, Y. Duan, L. Hou, Q. Zhou, C. Ma, X. Yang, R. Liu, F. Yang, L. Cui, C. Xu, Y. Li, *Appl. Catal. B*, **2017**, 203, 1–8.
[82] Y. Kofuji, Y. Isobe, Y. Shiraishi, H. Sakamoto, S. Tanaka, S. Ichikawa, T. Hirai, *J. Am. Chem. Soc.*, **2016**, 138, 10019–10025.
[83] L. Yan, Z. Gu, X. Zheng, C. Zhang, X. Li, L. Zhao, Y. Zhao, *ACS Catal.*, **2017**, 7, 7043–7050.
[84] Y. Chen, X. Xie, X. Xin, Z.-R. Tang, Y.-J. Xu, *ACS Nano*, **2019**, 13, 295–304.
[85] X. Ma, Q. Xiang, Y. Liao, T. Wen, H. Zhang, *Appl. Surf. Sci.*, **2018**, 457, 846–855.
[86] X.-H. Li, W.-L. Chen, H.-Q. Tan, F.-R. Li, J.-P. Li, Y.-G. Li, E.-B. Wang, *ACS Appl. Mater. Interfaces*, **2019**, 11, 37927–37938.
[87] J. Gu, Y. Yu, X. Fu, H. Chen, F. Jiang, X. Wang, *Appl. Surf. Sci.*, **2021**, 555, 149733.
[88] N. Zhang, M.-Q. Yang, Z.-R. Tang, Y.-J. Xu, *J. Catal.*, **2013**, 303, 60–69.
[89] N. Lv, Y. Li, Z. Huang, T. Li, S. Ye, D. D. Dionysiou, X. Song, *Appl. Catal. B*, **2019**, 246, 303–311.
[90] C. Bie, H. Yu, B. Cheng, W. Ho, J. Fan, J. Yu, *Adv. Mater.*, **2021**, 33, 2003521.
[91] H. Liu, Y. Liu, D. Zhu, *J. Mater. Chem.*, **2011**, 21, 3335–3345.
[92] F. Schedin, A. K. Geim, S. V. Morozov, E. W. Hill, P. Blake, M. I. Katsnelson, K. S. Novoselov, *Nat. Mater.*, **2007**, 6, 652–655.
[93] H. E. Romero, P. Joshi, A. K. Gupta, H. R. Gutierrez, M. W. Cole, S. A. Tadigadapa, P. C. Eklund, *Nanotechnology*, **2009**, 20, 245501.
[94] A. F. Gualdrón-Reyes, A. M. Meléndez, I. González, L. Lartundo-Rojas, M. E. Niño-Gómez, *J. Phys. Chem. C*, **2018**, 122, 297–306.
[95] P. Kuang, M. He, H. Zou, J. Yu, K. Fan, *Appl. Catal. B*, **2019**, 254, 15–25.
[96] M. Pedrosa, L. M. Pastrana-Martínez, M. F. R. Pereira, J. L. Faria, J. L. Figueiredo, A. M. T. Silva, *Chem. Eng. J.*, **2018**, 348, 888–897.
[97] M. Latorre-Sánchez, A. Primo, H. García, *Angew. Chem. Int. Ed.*, **2013**, 52, 11813–11816.
[98] Y. Yan, J. Gong, J. Chen, Z. Zeng, W. Huang, K. Pu, J. Liu, P. Chen, *Adv. Mater.*, **2019**, 31, 1808283.
[99] A. Bokare, S. Chinnusamy, F. Erogbogbo, *Catalysts*, **2021**, 11, 319.
[100] C. X. Guo, Y. Dong, H. B. Yang, C. M. Li, *Adv. Energy Mater.*, **2013**, 3, 997–1003.
[101] P. Huo, X. Shi, W. Zhang, P. Kumar, B. Liu, *J. Mater. Sci.*, **2021**, 56, 6031–6051.
[102] S. Zhuo, M. Shao, S.-T. Lee, *ACS Nano*, **2012**, 6, 1059–1064.
[103] J. Shen, Y. Zhu, C. Chen, X. Yang, C. Li, *Chem. Commun.*, **2011**, 47, 2580–2582.
[104] S. Min, J. Hou, Y. Lei, X. Ma, G. Lu, *Appl. Surf. Sci.*, **2017**, 396, 1375–1382.
[105] T.-F. Yeh, W.-L. Huang, C.-J. Chung, I. T. Chiang, L.-C. Chen, H.-Y. Chang, W.-C. Su, C. Cheng, S.-J. Chen, H. Teng, *J. Phys. Chem. Lett.*, **2016**, 7, 2087–2092.
[106] Y. Yan, J. Chen, N. Li, J. Tian, K. Li, J. Jiang, J. Liu, Q. Tian, P. Chen, *ACS Nano*, **2018**, 12, 3523–3532.
[107] Y. Xia, B. Cheng, J. Fan, J. Yu, G. Liu, *Small*, **2019**, 15, 1902459.
[108] M. Xing, W. Fang, X. Yang, B. Tian, J. Zhang, *Chem. Commun.*, **2014**, 50, 6637–6640.
[109] L. Chen, Y. Hernandez, X. Feng, K. Müllen, *Angew. Chem. Int. Ed.*, **2012**, 51, 7640–7654.
[110] L. Zhu, J. Wang, T. Zhang, L. Ma, C. W. Lim, F. Ding, X. C. Zeng, *Nano Lett.*, **2010**, 10, 494–498.

[111] M. Terrones, *ACS Nano*, **2010**, 4, 1775–1781.
[112] S. Darbari, V. Ahmadi, P. Afzali, Y. Abdi, *J. Phys. D: Appl. Phys.*, **2013**, 46, 385101.
[113] S. Ayissi, P. A. Charpentier, N. Farhangi, J. A. Wood, K. Palotás, W. A. Hofer, *J. Phys. Chem. C*, **2013**, 117, 25424–25432.
[114] Z. Han, L. Wei, H. Pan, C. Li, J. Chen, *J. Mol. Catal. A*, **2015**, 398, 399–406.
[115] F. Zhang, Y.-H. Li, J.-Y. Li, Z.-R. Tang, Y.-J. Xu, *Environ. Pollut.*, **2019**, 253, 365–376.
[116] L. Yuan, M.-Q. Yang, Y.-J. Xu, *J. Mater. Chem. A*, **2014**, 2, 14401–14412.
[117] X. Pan, M.-Q. Yang, Z.-R. Tang, Y.-J. Xu, *J. Phys. Chem. C*, **2014**, 118, 27325–27335.
[118] J. Sun, H. Zhang, L.-H. Guo, L. Zhao, *ACS Appl. Mater. Interfaces*, **2013**, 5, 13035–13041.
[119] D. Luo, Q. Zheng, Z. Zhang, Z. Guo, X. Wei, W. Zhen, X. Zhang, *Int. J. Hydrogen Energy*, **2019**, 44, 28123–28133.
[120] B. Ma, M. Blanco, L. Calvillo, L. Chen, G. Chen, T.-C. Lau, G. Dražić, J. Bonin, M. Robert, G. Granozzi, *J. Am. Chem. Soc.*, **2021**, 143, 8414–8425.
[121] N. H. Kwon, J. M. Lee, T.-H. Gu, X. Jin, S.-J. Hwang, *Sol. RRL*, **2021**, 5, 2000411.
[122] S. Wan, M. Ou, Q. Zhong, S. Zhang, F. Song, *Chem. Eng. J.*, **2017**, 325, 690–699.
[123] Y. Liang, Y. Chen, M. Zhao, L. Lin, R. Duan, Y. Jiang, J. Yan, Y. Wang, J. Zeng, Y. Zhang, *Catal. Sci. Technol.*, **2019**, 9, 6899–6908.
[124] P. Tan, A. Zhu, L. Qiao, W. Zeng, H. Cui, J. Pan, *J. Colloid Interface Sci.*, **2019**, 533, 452–462.
[125] P. Wang, S. Zhan, Y. Xia, S. Ma, Q. Zhou, Y. Li, *Appl. Catal. B*, **2017**, 207, 335–346.
[126] D. A. Reddy, R. Ma, T. K. Kim, *Ceram. Int.*, **2015**, 41, 6999–7009.
[127] Z. Mou, S. Yin, M. Zhu, Y. Du, X. Wang, P. Yang, J. Zheng, C. Lu, *Phys. Chem. Chem. Phys.*, **2013**, 15, 2793–2799.
[128] Q. Lang, Y. Chen, T. Huang, L. Yang, S. Zhong, L. Wu, J. Chen, S. Bai, *Appl. Catal. B*, **2018**, 220, 182–190.
[129] Y. Wang, J. Yu, W. Xiao, Q. Li, *J. Mater. Chem. A*, **2014**, 2, 3847–3855.
[130] G. Zhu, M. Hojamberdiev, S. Zhang, S. T. U. Din, W. Yang, *Appl. Surf. Sci.*, **2019**, 467–468, 968–978.
[131] A. Meng, L. Zhang, B. Cheng, J. Yu, *Adv. Mater.*, **2019**, 31, 1807660.
[132] M.-Y. Qi, Y.-H. Li, F. Zhang, Z.-R. Tang, Y. Xiong, Y.-J. Xu, *ACS Catal.*, **2020**, 10, 3194–3202.
[133] A. Li, X. Chang, Z. Huang, C. Li, Y. Wei, L. Zhang, T. Wang, J. Gong, *Angew. Chem. Int. Ed.*, **2016**, 55, 13618–13618.
[134] N. Zhang, Y. Zhang, Y.-J. Xu, *Nanoscale*, **2012**, 4, 5792–5813.
[135] Y.-H. Li, J.-Y. Li, Y.-J. Xu, *EnergyChem*, **2021**, 3, 100047.
[136] J. Kim, L. J. Cote, J. Huang, *Acc. Chem. Res.*, **2012**, 45, 1356–1364.
[137] N. Zhang, M.-Q. Yang, Z.-R. Tang, Y.-J. Xu, *ACS Nano*, **2014**, 8, 623–633.
[138] C. Han, M.-Q. Yang, N. Zhang, Y.-J. Xu, *J. Mater. Chem. A*, **2014**, 2, 19156–19166.
[139] A. W. Morawski, E. Kusiak-Nejman, A. Wanag, J. Kapica-Kozar, R. J. Wróbel, B. Ohtani, M. Aksienionek, L. Lipińska, *Catal. Today*, **2017**, 280, 108–113.
[140] Y. Shiraishi, S. Shiota, H. Hirakawa, S. Tanaka, S. Ichikawa, T. Hirai, *ACS Catal.*, **2017**, 7, 293–300.
[141] S. Pu, R. Zhu, H. Ma, D. Deng, X. Pei, F. Qi, W. Chu, *Appl. Catal. B*, **2017**, 218, 208–219.
[142] N. N. T. Ton, A. T. N. Dao, K. Kato, T. Ikenaga, D. X. Trinh, T. Taniike, *Carbon*, **2018**, 133, 109–117.
[143] H. Moussa, E. Girot, K. Mozet, H. Alem, G. Medjahdi, R. Schneider, *Appl. Catal. B*, **2016**, 185, 11–21.
[144] Y. Zhao, L. Liu, T. Cui, G. Tong, W. Wu, *Appl. Surf. Sci.*, **2017**, 412, 58–68.
[145] S. P. Lonkar, V. Pillai, A. Abdala, *Appl. Surf. Sci.*, **2019**, 465, 1107–1113.
[146] M. Maruthupandy, P. Qin, T. Muneeswaran, G. Rajivgandhi, F. Quero, J.-M. Song, *Mater. Sci. Eng. B*, **2020**, 254, 114516.
[147] S. Víctor-Román, E. García-Bordejé, J. Hernández-Ferrer, J. M. González-Domínguez, A. Ansón-Casaos, A. M. T. Silva, W. K. Maser, A. M. Benito, *Catal. Today*, **2020**, 357, 350–360.
[148] L. Tie, C. Yu, Y. Zhao, H. Chen, S. Yang, J. Sun, S. Dong, J. Sun, *J. Alloys Compd.*, **2018**, 769, 83–91.
[149] J. Wei, S. Xue, P. Xie, R. Zou, *Appl. Surf. Sci.*, **2016**, 376, 172–179.
[150] Y. Chen, F. Sun, Z. Huang, H. Chen, Z. Zhuang, Z. Pan, J. Long, F. Gu, *Appl. Catal. B*, **2017**, 215, 8–17.
[151] J. He, M. Zhang, A. Primo, H. García, Z. Li, *J. Mater. Chem. A*, **2018**, 6, 19782–19787.
[152] L. Allagui, B. Chouchene, T. Gries, G. Medjahdi, E. Girot, X. Framboisier, A. B. h. Amara, L. Balan, R. Schneider, *Appl. Surf. Sci.*, **2019**, 490, 580–591.
[153] J. Bian, J. Feng, Z. Zhang, J. Sun, M. Chu, L. Sun, X. Li, D. Tang, L. Jing, *Chem. Commun.*, **2020**, 56, 4926–4929.
[154] F.-X. Xiao, J. Miao, B. Liu, *J. Am. Chem. Soc.*, **2014**, 136, 1559–1569.
[155] S. Thakur, T. Kshetri, N. H. Kim, J. H. Lee, *J. Catal.*, **2017**, 345, 78–86.
[156] Y. Lu, X. Cheng, G. Tian, H. Zhao, L. He, J. Hu, S.-M. Wu, Y. Dong, G.-G. Chang, S. Lenaerts, S. Siffert, G. Van Tendeloo, Z.-F. Li, L.-L. Xu, X.-Y. Yang, B.-L. Su, *Nano Energy*, **2018**, 47, 8–17.
[157] Q. Zhao, J. Sun, S. Li, C. Huang, W. Yao, W. Chen, T. Zeng, Q. Wu, Q. Xu, *ACS Catal.*, **2018**, 8, 11863–11874.
[158] C. Xue, H. Li, H. An, B. Yang, J. Wei, G. Yang, *ACS Catal.*, **2018**, 8, 1532–1545.
[159] Q. Tian, W. Wu, J. Liu, Z. Wu, W. Yao, J. Ding, C. Jiang, *Dalton Trans.*, **2017**, 46, 2770–2777.
[160] R. Yang, K. Song, J. He, Y. Fan, R. Zhu, *ACS Omega*, **2019**, 4, 11135–11140.
[161] Y. Gao, B. Xu, M. Cherif, H. Yu, Q. Zhang, F. Vidal, X. Wang, F. Ding, Y. Sun, D. Ma, Y. Bi, Z. Xu, *Appl. Catal. B*, **2020**, 279, 119403.
[162] X. Li, X. Yan, X. Lu, S. Zuo, Z. Li, C. Yao, C. Ni, *J. Catal.*, **2018**, 357, 59–68.
[163] T. Wang, D. Yue, X. Li, Y. Zhao, *Appl. Catal. B*, **2020**, 268, 118399.
[164] Y.-H. Yao, J. Li, H. Zhang, H.-L. Tang, L. Fang, G.-D. Niu, X.-J. Sun, F.-M. Zhang, *J. Mater. Chem. A*, **2020**, 8, 8949–8956.
[165] Y. Zhang, Z.-R. Tang, X. Fu, Y.-J. Xu, *ACS Nano*, **2010**, 4, 7303–7314.
[166] J. Shen, G. Ma, J. Zhang, W. Quan, L. Li, *Appl. Surf. Sci.*, **2015**, 359, 455–468.
[167] M. Ahmad, E. Ahmed, Z. L. Hong, J. F. Xu, N. R. Khalid, A. Elhissi, W. Ahmed, *Appl. Surf. Sci.*, **2013**, 274, 273–281.
[168] A. A. Ashkarran, B. Mohammadi, *Appl. Surf. Sci.*, **2015**, 342, 112–119.
[169] M. Long, Y. Qin, C. Chen, X. Guo, B. Tan, W. Cai, *J. Phys. Chem. C*, **2013**, 117, 16734–16741.
[170] X. Pan, M.-Q. Yang, Y.-J. Xu, *Phys. Chem. Chem. Phys.*, **2014**, 16, 5589–5599.
[171] H. Zhang, X. Lv, Y. Li, Y. Wang, J. Li, *ACS Nano*, **2010**, 4, 380–386.
[172] K. M. Cho, K. H. Kim, K. Park, C. Kim, S. Kim, A. Al-Saggaf, I. Gereige, H.-T. Jung, *ACS Catal.*, **2017**, 7, 7064–7069.
[173] B. Bajorowicz, J. Reszczyńska, W. Lisowski, T. Klimczuk, M. Winiarski, M. Słoma, A. Zaleska-Medynska, *RSC Adv.*, **2015**, 5, 91315–91325.

[174] R.-X. Wang, Q. Zhu, W.-S. Wang, C.-M. Fan, A.-W. Xu, *New J. Chem.*, **2015**, 39, 4407–4413.

[175] X. Li, S. Wang, L. Li, Y. Sun, Y. Xie, *J. Am. Chem. Soc.*, **2020**, 142, 9567–9581.

以石墨烯作用为导向的多功能石墨烯基复合光催化剂

李月华, 唐紫蓉*, 徐艺军#

福州大学化学学院, 能源与环境光催化国家重点实验室, 福建福州350116

摘要: 具有单层二维蜂窝状结构的石墨烯在材料科学和能源转化领域吸引了巨大的研究兴趣. 在光催化领域, 因其独特的二维平面结构、优异的电荷传输能力、超高的理论比表面积、良好的透光性和化学稳定性, 可作为高效的助催化剂, 以提高光催化体系的太阳能转换效率. 在一些特定的光催化体系中, 石墨烯还可以作为大分子光敏剂产生光生电子. 近年来, 石墨烯基复合光催化剂, 如石墨烯-半导体、石墨烯-金属和石墨烯-有机物复合材料, 已被广泛应用于光催化水分解制氢、环境净化、二氧化碳还原和选择性有机合成, 为缓解能源与环境问题提供了一种有效策略.

众所周知, 合成方法对石墨烯基复合光催化剂的形貌、尺寸、缺陷结构、表界面性质等影响很大, 这些性质与石墨烯基复合光催化剂的催化性能密切相关. 因此, 探索合适的合成方法制备具有目标功能结构的高效石墨烯基复合光催化剂, 具有重要的科学意义. 现有的合成方法主要包括: 水热/溶剂热法、煅烧法、低温油浴法、溶胶-凝胶法、超声辅助沉积法、微波辅助合成法、电化学沉积法、光化学还原法等. 根据概念进行归类, 可分为非原位合成法和原位合成法.

在非原位合成中, 预制的光活性材料的形貌和尺寸保持不变, 有利于实现对石墨烯基复合光催化剂微观结构的精确控制, 以及对空白光活性组分和复合光催化剂性能进行比较. 在原位合成中, 石墨烯或其前驱体不仅可以作为二维模板调控纳米晶的成核和生长, 合成具有可控形貌和良好界面接触的石墨烯基复合光催化剂, 还可以作为三维石墨烯凝胶的自组装模板. 此外, 氧化石墨烯作为常用的石墨烯前驱体, 可以同时作为模板和表面活性剂, 灵活调控一些特定复合材料的形貌、尺寸和缺陷结构等.

鉴于已有大量综述系统地总结了石墨烯基复合光催化剂的分类、合成方法、性质和应用等, 本文先介绍石墨烯基复合光催化剂的优化策略, 例如降低石墨烯的缺陷密度、化学掺杂、优化维数、沉积助催化剂、优化界面参数; 再以石墨烯在光催化中的基本作用为导向, 讨论石墨烯基复合光催化剂的合成. 最后, 对石墨烯基复合催化剂在光催化领域面临的挑战和优化策略进行了展望, 希望为多功能石墨烯基复合光催化剂的合理制备及高效利用提供参考.

关键词: 石墨烯; 复合光催化剂; 优化策略; 合成方法; 石墨烯的多重作用; 光催化应用

收稿日期: 2021-05-07. 接受日期: 2021-06-27. 上网时间: 2022-02-03.

*通讯联系人. 电子信箱: zrtang@fzu.edu.cn

#通讯联系人. 电话: (0591)22865836; 电子信箱: yjxu@fzu.edu.cn

基金来源: 国家自然科学基金(22072023, 21872029, U1463204, 21173045); 国家万人计划科技创新领军人才(00387072); 闽江学者特聘教授奖励计划; 福建省首批青年拔尖创新人才和福建省自然科学基金(2017J07002和2019J0106).

本文的电子版全文由Elsevier出版社在ScienceDirect上出版(http://www.sciencedirect.com/journal/chinese-journal-of-catalysis).